Master Thesis

Observational Studies on Magnetic Helicity Associated with Solar Flares

Takahiro Hasegawa

Space and Planetary Science Group

Department of Earth and Planetary Science

Graduate School of Science, The University of Tokyo

February 27, 2018

Abstract

Solar flares are explosive phenomena caused by magnetic reconnection. Excessive energy (called free energy) is stored in complex magnetic field and released through a flare. When, where and how free energy is stored and released is one of the most important issues in solar physics. Moreover, the trigger process of solar flares is also a relevant open question. In the present, it is argued that magnetic helicity which quantifies the complexity of the magnetic field has an important role on the energy build-up and triggering flares. Therefore, we study the evolution of the magnetic field and magnetic helicity in a flare-productive active region named NOAA 12297. In this region, 10 M-class flares and 1 X-class flare are observed by the Atmospheric Imaging Assembly on board the Solar Dynamics Observatory (SDO) from 12UT on 2015 March 10th to 12UT on 13th. NOAA 12297 had 2 regions which showed different patterns of flare occurrences. In the eastern region (named Region 1 in this work) produced 2 M-class flares and 1 X-class flare. Whereas, the western region (named Region 2) produced 7 M-class flares.

We estimate the magnetic helicity injection and its spatial distribution in the active region with data obtained by the Helioseismic Magnetic Imager on board the SDO. We also evaluate contributions of self rotation of a sunspot and mutual rotation between a sunspot and emerging fluxes with spinning and braiding helicity injection. Furthermore, we perform NLFFF extrapolation using the magnetic field data obtained by Solar Optical Telescope/Spectro-Polarimeter on board $Hinode$, and discuss the topology of the 3-dimensional magnetic field.

Region 1 and 2 had a similar configuration; emerging fluxes moving counter-clockwise

to a sunspot. We find that, although positive magnetic helicity was mainly accumulated monotonically in NOAA 12297 on the whole, the increase stopped before the X-class flare occurred. This was due to negative helicity injection in a sunspot which started soon after flux emergence in Region 1. Moreover, negative spinning helicity injection in the sunspot was larger than braiding helicity injection. Meanwhile, generally positive magnetic helicity was injected in Region 2. The most significant feature in Region 2 was fluctuating time profile of braiding helicity injection.

We consider that the negative spinning helicity injection was due to the reversal of the sunspot's rotation in Region 1, and this reversed rotation was forced by flux emergence. This argument is consistent with the flare model of helicity annihilation that the X-class flare occurred after opposite helicity injection. On the other hand, oscillating braiding helicity injection in Region 2 implies a recurrent energy input. This is also consistent with the fact that Region 2 produced M-class flares successively.

要旨

太陽フレアは磁気リコネクションによっておこる爆発現象である。フレアによって、複雑な磁場に蓄えられた余剰なエネルギー (自由エネルギーと呼ばれる) が解放される。しかし、自由エネルギーがいつ、どこで、どのように蓄積されるのかということについては、フレア研究における長年の問題である。また、フレアのトリガー機構の解明も未だ為されていない。これらの問題に対して、磁場の複雑さの定量化である磁気ヘリシティが重要な意味を持っていることが、近年の研究から示唆されている。そこで本論文では、フレアが頻発した活動領域である NOAA 12297 における磁場と磁気ヘリシティの発展について研究した。本領域においては、太陽観測衛星「Solar Dynamics Observatory(SDO)」に搭載されている観測装置「Atmospheric Imaging Assembly」によって、2015 年 3 月 10 日 12 時 UT から 13 日 12 時 UT の間に 10 回の M クラスフレアと 1 回の X クラスフレアが観測されている。また、特に活動的な東側領域 (Region 1) と西側領域 (Region 2) におけるフレア発生の傾向は、前者では 2 回の M クラスフレアと 1 回の X クラスフレア、後者では 7 回の M クラスフレアというように異なる振る舞いを見せた。

本研究では、「SDO」に搭載された磁場測定装置「Helioseismic Magnetic Imager」で得られた磁場データを用いて、コロナへの磁気ヘリシティ入射量と空間分布を計算した。さらに、Region 1 と 2 において、黒点自身の回転あるいは黒点-浮上磁場間の相互の回転の寄与を Spinning helicity injection と Braiding helicity injection を用いて評価した。加えて、太陽観測衛星「ひので」に搭載されている「Solar Optical Telescope/Spectro-Polarimeter」によって得られた磁場データを用いた NLFFF 外挿計算によって 3 次元コロナ磁場を再現し、そのトポロジーについて議論した。

両領域における磁場発展の様子は類似しており、ともに黒点に対して浮上磁場が反時計回りに運動していた。活動領域全体では、基本的には正の磁気ヘリシティが単調増加的に蓄積していたが、X クラスフレア発生前に増加が止まった。これは Region 1 の黒点における負のヘリシティ入射と対応しており、この時 Region 1 では Braiding helicity injection よりも負の Spinning helicity injection の寄与が支配的であった。一方で、Region 2 においては、基本的に正のヘリシティが入射しており、変動的な正の Braiding helicity injection が支配的であった。

Region 1 における負のヘリシティ入射は、磁場浮上によって起こされた黒点の逆回転によるものと考えられる。X クラスフレア発生前の逆極性のヘリシティ入射は、正負のヘリシティの対消滅によりフレアが駆動されるというモデルと整合的である。一方、Region 2 における変動的な Braiding helicity injection は、回帰的なエネルギー・インプットを示唆しており、M クラスフレアの連続的な発生と合致している。

Contents

Chapter 1

Introduction

Since the first observation of the Sun by Galilei with his telescope, the star and its activity have attracted many astronomers and physicists. The Sun is covered with magnetic field generated in the solar interior by the so-called solar dynamo, and various interactions between magnetic field and a plasma cause a myriad of features. The most prominent activity is a solar flare, which is the largest explosive phenomenon in our solar system and the central phenomenon of this thesis. For this reason, in the present chapter, we overview some topics and previous theoretical and observational studies on solar flares.

1.1 Solar Flares

Solar flares are explosive brightening phenomena occurring at the solar atmosphere. Solar flares are understood as releasing process of excessive magnetic energy stored in the solar corona, called "free energy", by magnetic reconnection converting free energy into various forms (e.g. radiative, kinetic, and thermal). The released energy by a flare amounts to $10^{29} \sim 10^{32}$ erg. They have been studied theoretically and observationally. It is considered that various features of flares are caused by magnetic reconnection. Fig. 1.1 shows the Ca II H image of the X3.4 flare at 2006 December 13th obtained by the Solar Optical Telescope (SOT) Filtergram (FG) on board the $Hinode$ satellite. Two ribbon-like brightening called as flare ribbons are formed by heat input to the chromosphere from the

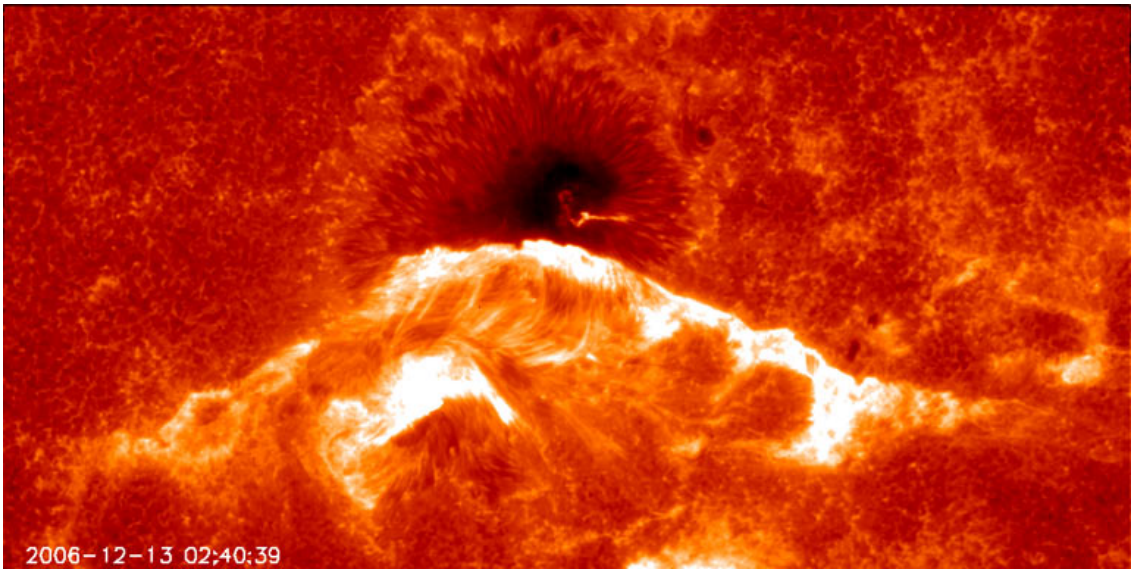

Figure 1.1: Flare ribbons seen in the Ca II H line on 2006 December 13th observed by $Hinode$ SOT/FG.

X-point where magnetic reconnection takes place. Right figure in Fig. 1.2 shows X-ray images of the solar flare, which occurred at 2017 September 10th, obtained by the X-Ray Telescope (XRT) on board the $Hinode$. The upper image shows that the plasmoid structure was ejected soon after this flare occurred. The current sheet was elongated around the X-point. In the gradual (later) phase, the cusp-shaped post flare loop grew. As shown in the left cartoon in fig. 1.2, the most standard 2D model of a flare called as the CSHKP model (Carmichael, 1964; Sturrock, 1966; Hirayama, 1974; Kopp & Pneuman, 1976) explains these features. Flares are classified into A, B, C, M, and X-class according to a magnitude of intensity of soft X-ray (1 - 8Å) obtained by the Geostationary Environmental Satellite (GOES). This classification is described in table 1.1.

Class	Intensity of Soft X-ray Emission [$erg\ cm^{-2}\ s^{-1}$]
A	$< 10^{-5}$
B	$10^{-4} \sim 10^{-3}$
C	$10^{-3} \sim 10^{-2}$
M	$10^{-2} \sim 10^{-1}$
X	$> 10^{-1}$

Table 1.1: Definition of classes of solar flares in accordance with GOES soft X-ray (1 - 8Å) intensity.

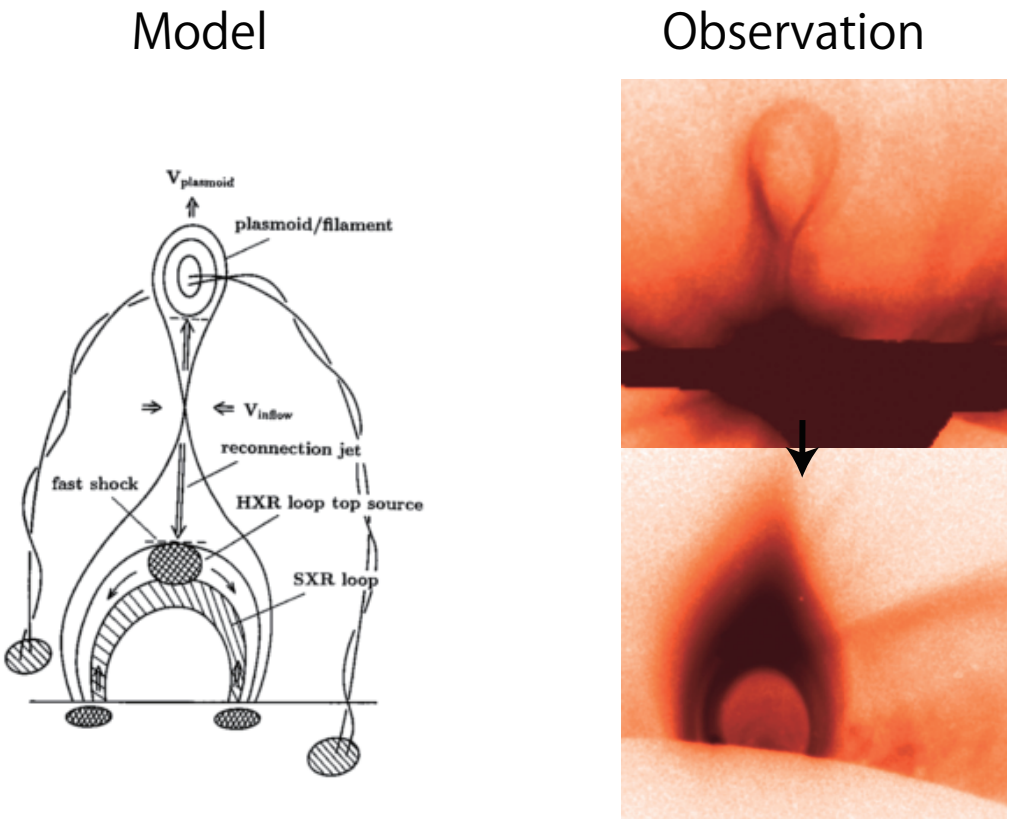

Figure 1.2: (Left) Schematics of CSHKP model from Shibata et al. (1995). This is the most standard model of 2D magnetic reconection of a flare. (Right) X-ray images of X-class flare occurred in 2017 September 10th obtained by *Hinode* XRT. (Right top) The structure of plasmoid was ejected when the flare started and (Right bottom) in the late phase, post flare loop grew. The schematic model and observed features are quite similar.

1.2 Free Energy and Magnetic Helicity

1.2.1 Complex Topology of Solar Magnetic Field

Previous observations revealed the complex 3-dimensional structure of the coronal magnetic field. Since the plasma having high magnetic Reynolds number is frozen in magnetic field, brightening features seen in the EUV and X-ray bands depict the topology of the coronal magnetic field. X-ray sigmoid (fig. 1.3(a)) and helical motions of filament eruption (fig. 1.3(c)) are features implying complex topology of coronal magnetic field. X-ray sigmoid is S- or inverse S-shaped bright structure seen in the soft X-ray band as shown in fig.1.3(a). This structure has been considered as a precursor of a large flare. Fig 1.3(c) shows filament eruption with the helical motion observed in the EUV band. One of the promising mechanisms for explaining the drivers of solar eruptions is the kink instability (Sturrock et al., 2001). When a highly twisted flux rope is perturbed, a concave part has stronger magnetic pressure than a convex part because of the imbalance of the poloidal magnetic field which is enhanced by the twist. Therefore, when the twist is beyond a critical condition, the flux rope becomes unstable. This mechanism is called kink instability. Fig 1.3 (b) and (d) show the numerical modeling of sigmoid and kink instability, respectively. These phenomena imply that dynamic activities and instabilities in the solar atmosphere are strongly related to twisted and complex magnetic field topology.

The origin of free energy released through solar flares is understood as the complex (i.e. non-potential) configuration of coronal magnetic field. To evaluate this quantitatively, free energy W_{free} is defined as the excessive energy of magnetic field $\mathbf{B}$ compared to the non-current potential field $\mathbf{B_P}$;

$$W_{Free} = E(\mathbf{B}) - E(\mathbf{B_P}) \tag{1.1}$$

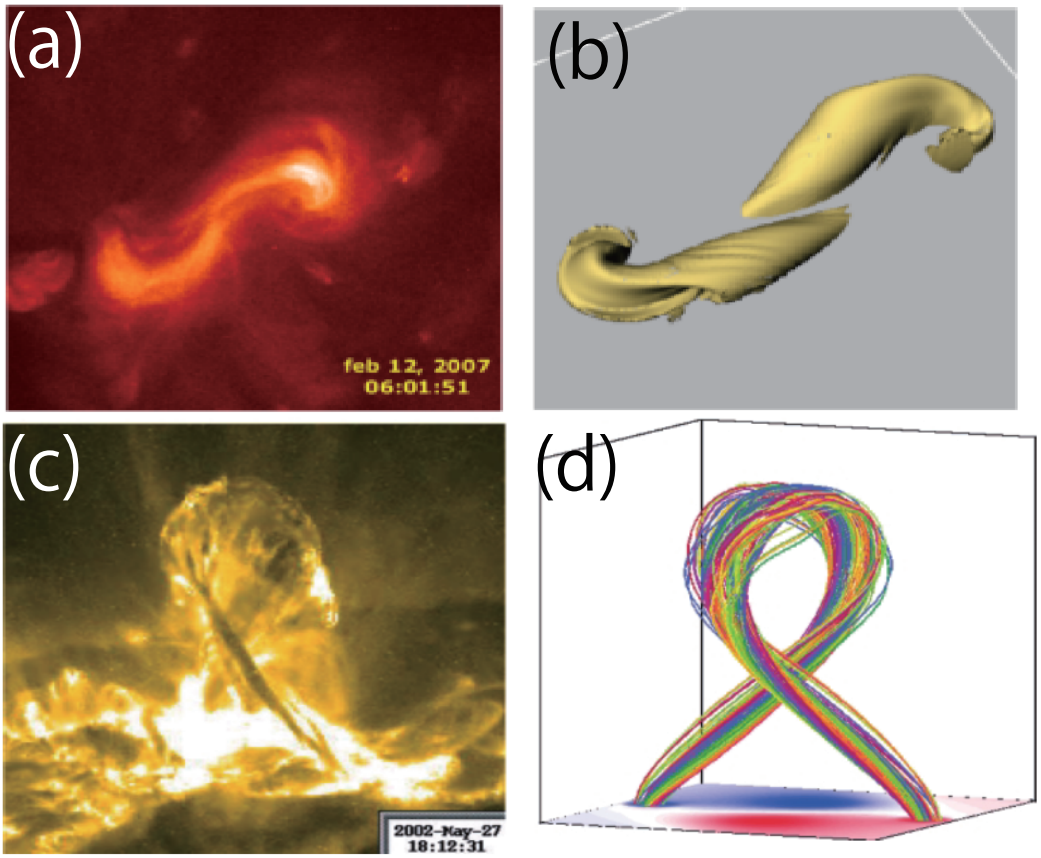

Figure 1.3: Observed features of complex magnetic field and reproductions of these phenomena with numerical modeling. (a) X-ray sigmoid observed by *Hinode* XRT. (b) Numerical modeling of sigmoid. Yellow surface stands for the constant current surface. ((a) and (b) are from Archontis et al. (2009).) (c) The image of confined filament eruption in 195 Å observed by the TRACE. (d) Magnetic field modeling of kink-unstable flux rope. ((c) and (d) are from Török & Kliem (2005).)

where

$$E(\mathbf{B}) = \frac{B^2}{2\mu_0} \tag{1.2}$$

$$\mathbf{B_P} = \nabla\Psi, \tag{1.3}$$

μ_0 is the permeability of a vacuum, and Ψ is an arbitrary scalar potential. Equilibrium of coronal magnetic structure is achieved only by the Lorentz force (which is force-free equilibrium) because gas pressure and gravitational force are much smaller than the Lorentz force in the corona then can be neglected. Thus the condition of dynamical equilibrium can be written as

$$\mathbf{B} \times \mathbf{J} = 0, \tag{1.4}$$

in another form,

$$\nabla \times \mathbf{B} = \alpha(\mathbf{x})\mathbf{B} \tag{1.5}$$

where $\mathbf{J} = \nabla \times \mathbf{B}/2\mu_0$ is electric current and $\alpha(\mathbf{x})$ is the coefficient called "force-free alpha" which generally depends on the position $\mathbf{x}$. This force-free condition is achieved well in the low-β plasma such as the corona (Gary, 2001). Magnetic field satisfying this force-free condition is called as "nonlinear force-free field (NLFFF)". When α is constant at any position, such structure is called as "linear force-free field (LFFF)". Note that, however, the plasma in the photosphere does not satisfy the force-free condition well because gas pressure is large, then cannot be neglected. The above-mentioned coronal atmospheric condition implies that the coronal magnetic field is subject to the evolution of photospheric magnetic field. This means that when photospheric magnetic field changes, the information of the fluctuation travels in a form of the Alfvén wave toward the corona. Since the Alfvén velocity is much faster in the solar atmosphere (e.g., $\sim$ 10km/s in the photosphere and $\sim$ 1000km/s in the corona) than the timescale of the photospheric evolu-

tion ($\sim$ 1km/s), the coronal magnetic field immediately responds to the photospheric fluctuation and satisfies the dynamical equilibrium state. Through this process, the coronal magnetic field stores free energy and complexity. Therefore, the coronal field becomes the high energy state following photospheric evolution and keeping dynamical equilibrium. When a flare occurs, the accumulated energy is released and the magnetic field relaxes to simple structure.

1.2.2 Formulation of Magnetic Helicity

Magnetic helicity H quantifies complexity of twisted, knotted, and linked magnetic field structure. Magnetic helicity H in a simply connected volume V whose boundary ∂V is the magnetic surface (i.e. $\mathbf{B} \cdot \hat{\mathbf{n}} = 0$ at ∂V, where "n" means the normal direction) is defined as

$$H = \int_V \mathbf{A} \cdot \mathbf{B} dV \tag{1.6}$$

where $\mathbf{B}$ stands for magnetic field vector and $\mathbf{A}$ is its vector potential. H is a gauge-invariant quantity as shown in Section 1.2.3. Magnetic helicity defined in Eq. (1.6) is a fundamental quantity for laboratory plasma covered by a conducting wall satisfying $\mathbf{B} \cdot \hat{\mathbf{n}} = 0$ (e.g. the RFP and Tokamak).

This definition of magnetic helicity, however, cannot be applied to the solar corona directly. When we consider the complexity of coronal magnetic field, we have to take the volume V whose surface contains the photosphere where $\mathbf{B} \cdot \hat{\mathbf{n}} \neq 0$. The quantity H defined in the volume changes its value depending on the gauge. To apply magnetic helicity to the solar corona as well as the laboratory, we can consider relative magnetic helicity H_R defined in the volume V whose boundary ∂V does not need to be a magnetic surface as

$$H_R = \int_V \mathbf{A} \cdot \mathbf{B} dV - \int_V \mathbf{A}_{\mathbf{ref}} \cdot \mathbf{B}_{\mathbf{ref}} dV \tag{1.7}$$

where $\mathbf{B_{ref}}$ is reference magnetic field satisfying $\mathbf{B_{ref}} \cdot \mathbf{n} = \mathbf{B} \cdot \mathbf{n}$ at ∂V, and $\mathbf{A_{ref}}$ is its vector potential (Berger & Field, 1984). Note that relative magnetic helicity is also gauge-invariant. When we choose potential field as reference field, relative helicity can be defined only by $\mathbf{B}$ (Finn & Antonsen Jr., 1985). In this case, relative helicity is defined as

$$H_R = \int_V (\mathbf{A} + \mathbf{A_P}) \cdot (\mathbf{B} - \mathbf{B_P}) dV \tag{1.8}$$

where $\mathbf{A_P}$ stands for the vector potential of $\mathbf{B_P}$. Hereafter, the term 'magnetic helicity' stands for the relative magnetic helicity defined as Eq. (1.8).

Now we consider V defined as following: ∂V is constituted of S_p penetrated by magnetic field (standing for the photosphere) and a magnetic surface S_o (the rest part of ∂V). Temporal evolution of magnetic helicity in volume V can be written as

$$\frac{dH_R}{dt} = \frac{dH_R}{dt}\Big|_{S_p} + \frac{dH_R}{dt}\Big|_{S_o} + \frac{dH_R}{dt}\Big|_{dis} \tag{1.9}$$

where $dH_R/dt\Big|_{S_p}$ is the injection term through the photosphere, $dH_R/dt\Big|_{S_o}$ is the injection (or ejection) term through S_o and $dH_R/dt\Big|_{dis}$ is the dissipation term. The dissipation term $dH_R/dt\Big|_{dis}$ can be neglected because magnetic helicity cascades to the large scale in which turbulent dissipation is small. $dH_R/dt\Big|_{S_o}$ is attributed to ejections of the plasma and magnetic field such as coronal mass ejections (CMEs) and solar wind. This term cannot be estimated accurately with the current observational approach because magnetic field vector and velocity field cannot be deduced. We, therefore, do not consider this term. Hence, we consider the time derivative of magnetic helicity as helicity injection through the photosphere into the corona;

$$\frac{dH_R}{dt}\Big|_{S_p} = 2\int [\mathbf{A_P} \times (\mathbf{v} \times \mathbf{B})]_n dS_p \tag{1.10}$$

$$= 2\int [(\mathbf{A_P} \cdot \mathbf{B_t}) v_n - (\mathbf{A_P} \cdot \mathbf{v_t}) B_n] dS_p \tag{1.11}$$

where the subscript "n" and "t" stand for the normal and transverse component, respectively. To calculate this quantity, not only the photospheric magnetic field but also photospheric velocity field are needed. The latter term of helicity injection rate in a active region was estimated for the first time by Chae et al. (2001) using the optical flow method "Local Correlation Tracking" (LCT, November & Simon (1988)). Kusano et al. (2002) developed the algorithm to derive not only horizontal but also vertical velocity field at the photosphere and estimated magnetic helicity injection rate by emerging and shearing motions separately. Démoulin & Berger (2003) suggested that velocity field which can be obtained with a optical flow method is "footpoint velocity field **u**" (see fig 1.4) ;

$$\mathbf{u} = \mathbf{v}_t - \frac{v_n}{B_n}\mathbf{B}_t. \tag{1.12}$$

With the footpoint velocity, helicity injection rate can be written as

$$\frac{dH_R}{dt} = -2\int_S (\mathbf{A_P}\cdot\mathbf{u})B_n dS. \tag{1.13}$$

Then, the magnetic helicity and its distribution in an active region have been studied based on formulation of Eq. (1.13). However, when we consider the integrand of relative helicity injection as helicity flux density, this definition produce a strong spurious signal of fake polarity, because magnetic helicity injection is gauge-invariant only when it is surface-integrated. Suggesting an alternative approach, Pariat et al. (2005) defines the magnetic helicity flux density G_θ, written as

$$G_\theta(\mathbf{x}) = -\frac{B_n(\mathbf{x})}{2\pi}\int_{S'}\frac{d\theta(\mathbf{x}-\mathbf{x}')}{dt}B'_n(\mathbf{x}')dS'. \tag{1.14}$$

Here $d\theta(\mathbf{x}-\mathbf{x}')/dt$ is defined as

$$\frac{d\theta(\mathbf{x}-\mathbf{x}')}{dt} = \frac{(\mathbf{x}-\mathbf{x}')\times(\mathbf{u}(\mathbf{x})-\mathbf{u}'(\mathbf{x}'))}{|\mathbf{x}-\mathbf{x}'|^2}\cdot\mathbf{n} \tag{1.15}$$

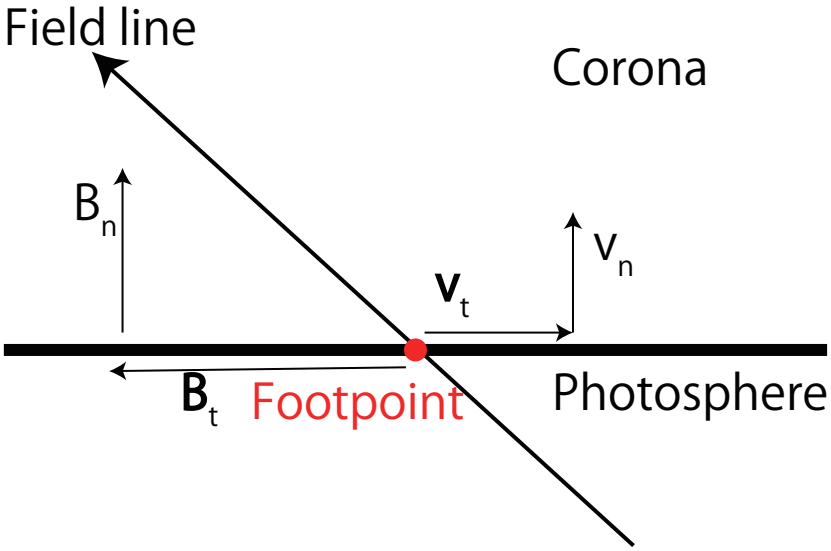

Figure 1.4: The schematics of the foot point velocity $\mathbf{u}$ suggested by Démoulin & Berger (2003). The footpoint motion of photospheric magnetic flux is contributed by horizontal motion and the apparent motion of the cross section of the rising flux tube.

standing for the relative rotation of $\mathbf{x}'$ to $\mathbf{x}$ as shown fig 1.5. Eq.(1.14) and (1.15) mean that magnetic helicity injection at the position $\mathbf{x}$ is superposition of relative rotation of $\mathbf{x}'$ to $\mathbf{x}$ weighted by vertical magnetic field at both positions, $B_n(\mathbf{x})$ and $B'_n(\mathbf{x}')$. Surface-integration of G_θ can be related to helicity injection in the surface;

$$\frac{dH_R(t)}{dt} = \int_S G_\theta(\mathbf{x}, t) dS. \tag{1.16}$$

1.2.3 Important Properties of Magnetic Helicity

Here, we summarize important properties of magnetic helicity. The properties are very favorable for studies of solar flares.

First, magnetic helicity can be used as a proxy of free energy, because free energy is stored as complexity of magnetic field. Actually, when magnetic field is in the relaxed LFFF state (Taylor state; Taylor 1974), magnetic helicity H and free energy W_{free} have

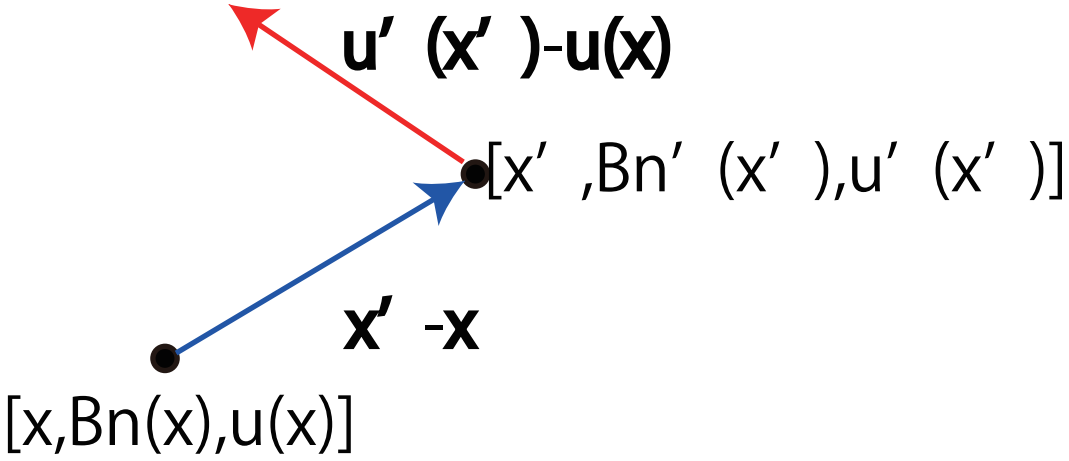

Figure 1.5: Schematics of relative rotation of $\mathbf{x}'$ to $\mathbf{x}$ in the definition of $d\theta(\mathbf{x}-\mathbf{x}')/dt$.

the following relation (Kusano et al., 1995),

$$\frac{dW_{free}}{dH} = \frac{\alpha}{2\mu_0}. \tag{1.17}$$

Second, magnetic helicity is a well-conserved quantity in a plasma having high magnetic Reynolds number in the corona. Since the plasma is frozen in the magnetic field in such a condition, field lines cannot pass through each other and the topology of magnetic field does not change if there are not special mechanisms as magnetic reconnection. Moreover, magnetic helicity is a robust quantity even considering dissipative processes such as magnetic reconnection (Matthaeus, 1982). As mentioned in the previous section, magnetic energy cascades to small scale in which dissipation works effectively, whereas magnetic helicity cascades to large scale and is not affected by the small-scale turbulent dissipation (Frisch et al., 1975; Pouquet et al., 1976). Thanks to this conservation property, accumulated magnetic helicity in the corona can be estimated with magnetic helicity injection at the photosphere. Consequently, magnetic helicity can be regarded as more robust quantity than free energy.

Third, magnetic helicity is a gauge-invariant quantity. Since the definition of magnetic helicity is related to the vector potential $\mathbf{A}$, we can consider the gauge transformation $\mathbf{A}+\mathbf{A_P} \rightarrow \mathbf{A}+\mathbf{A_P}+\nabla\chi$ where χ is an arbitrary scalar function. This transformation

modifies the form of magnetic helicity as

$$H' = \int_V (\mathbf{A} + \mathbf{A_P} + \nabla\chi) \cdot (\mathbf{B} - \mathbf{B_P}) dV. \tag{1.18}$$

The difference between H and H' is

$$H' - H = \int_V (\nabla\chi) \cdot (\mathbf{B} - \mathbf{B_P}) dV \tag{1.19}$$

$$= \int_V \nabla \cdot [\chi(\mathbf{B} - \mathbf{B_P})] dV - \int_V \chi[\nabla \cdot (\mathbf{B} - \mathbf{B_P})] dV. \tag{1.20}$$

The second term vanishes bacause $\nabla \cdot \mathbf{B} = 0$ and $\nabla \cdot \mathbf{B_P} = 0$. The first term is;

$$\int_V \nabla \cdot [\chi(\mathbf{B} - \mathbf{B_P})] dV = \int_{\partial V} [\chi(\mathbf{B} - \mathbf{B_P})] \cdot \mathbf{n} d\partial V = 0 \tag{1.21}$$

because $\mathbf{B} \cdot \mathbf{n} = \mathbf{B_P} \cdot \mathbf{n}$ on ∂V. Consequently the gauge transformation does not change the value of magnetic helicity.

Finally, although the coronal magnetic helicity cannot be estimated directly because there are no available measurement of the coronal magnetic field, the helicity injection into the corona through the photosphere can be calculated with Eq. (1.13). Therefore we can determine the temporal evolution of coronal magnetic helicity, namely, coronal energetic state. This property is very convenient in the situation where the magnetic field can be observed only at the photosphere.

1.2.4 Hemispheric Rule of Magnetic Helicity

It is suggested that the sign of the magnetic helicity has hemispheric preference independent of the solar cycles (Pevtsov, 1995). Negative and positive helicity tend to be generated dominantly in the northern and southern hemisphere, respectively. This sign preference is called "hemispheric rule" and is attributed to the Coriolis force (Holder et al., 2004), $\Sigma-$effect (Longcope et al., 1999), and differential rotation of the Sun (Démoulin

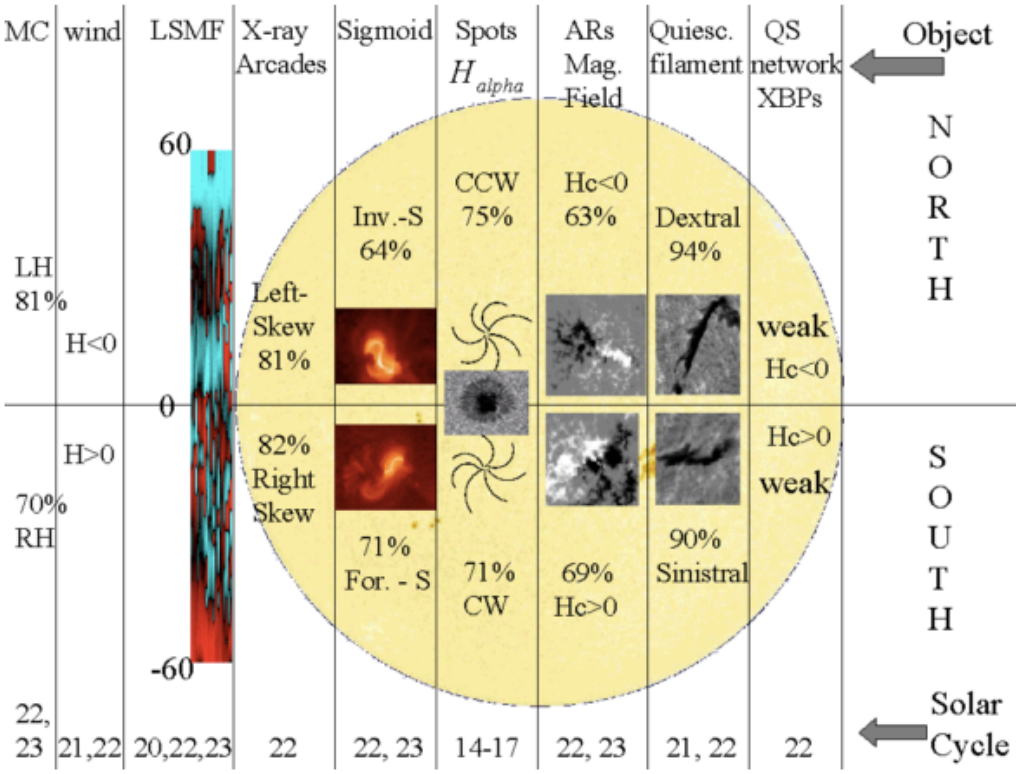

Figure 1.6: The summary of hemispheric sign preference, reprinted from Pevtsov (2002).

et al., 2002).

As summarized in fig. 1.6, this preference has been discovered in various phenomena, e.g., the quiet sun network field, X-ray bright points, quiescent filaments, active region magnetic field, magnetic field configuration in a sunspot, a shape of a sigmoid, X-ray arcade overlying quiescent filaments, large scale magnetic field (LSMF), solar wind and magnetic clouds (Pevtsov, 2002). For example, inverse S-shaped sigmoids are observed more frequently than S-shaped sigmoids in the northern hemisphere, while S-shaped sigmoids are observed more frequently in the southern hemisphere. Spiral configuration of a sunspot weakly depends on the hemisphere; counter clockwise spiral can be seen more in the northern hemisphere and clockwise in the southern hemisphere.

1.3 Sunspot Rotation

One of the important photospheric features related to the injection of magnetic helicity into the corona is sunspot rotation.

Many previous works reported that sunspots show rotational motion. Evershed (1909, 1910) first presented the evidence of sunspot rotation by spectral observation. Sunspot rotation is thought to be an important mechanism to energize the corona and to initiate solar flares and CMEs. Stenflo (1969) and Barnes & Sturrock (1972) showed that the sunspot rotation can build-up sufficient free energy for producing a flare. Additionally, some previous works discussed the role of the sunspot rotation on energy build-up for flares in more detail (Amari et al., 1996; Tokman & Bellan, 2002; Torok & Kliem, 2003). Some studies investigated the relationship between sunspot rotation and flare productivity (Régnier & Canfield, 2006; Yan et al., 2008; Zhang et al., 2008; Suryanarayana, 2010), effects on the corona (Brown et al., 2003; Tian & Alexander, 2006, 2008), non-potential parameters (Zhang et al., 2007; Kazachenko et al., 2010; Vemareddy et al., 2012), and helicity injection (Ravindra et al., 2011; Vemareddy et al., 2012). Yan et al. (2008) classified sunspot pairs into six groups based on the features of their self and mutual rotations. The authors concluded that sunspot rotation against differential rotation tends to produce larger flares.

Some works discussed the mechanism of sunspot rotation (Longcope & Welsch, 2000; Chae et al., 2003; Gibson et al., 2004; Magara, 2006; Fan, 2009; Sturrock et al., 2015; Sturrock & Hood, 2016). Min & Chae (2009) suggested two explanations of mechanisms of sunspot rotation. One explanation is that sunspot rotation is the apparent motion of twisted magnetic tube rising vertically. The other explanation is that, when twisted flux emerges into the corona, it drastically expands due to the difference of pressure between the interior and the corona. The expansion generates the imbalance of the torque, it drives photospheric plasma to rotate, and the rotation transports magnetic helicity (see fig. 1.7). The latter explanation is based on Longcope & Welsch (2000) and Chae et al. (2003).

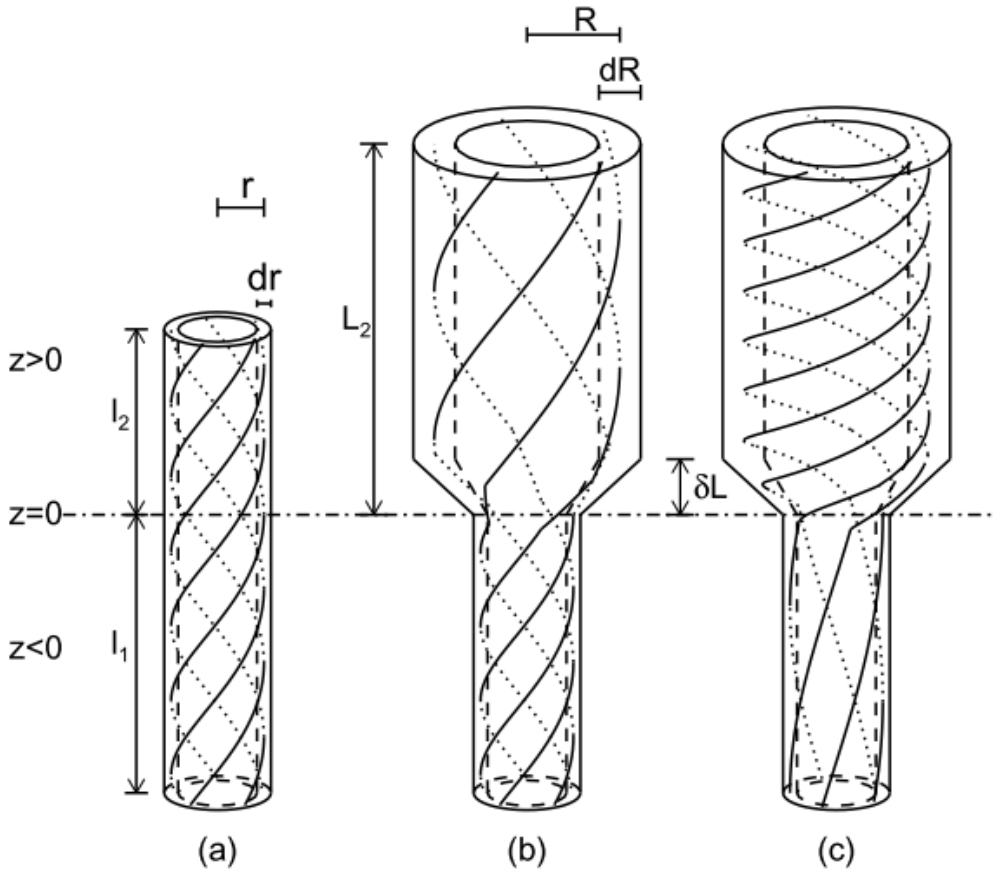

Figure 1.7: Schematics of sunspot rotation driven by the expansion and the imbalance of the torque, from Chae et al. (2003).

Though it is difficult to tell which mechanism attributes to observed sunspot rotation, Sturrock et al. (2015) explained sunspot rotation by the imbalance of the torque rather than the apparent motion.

Sunspot rotation is considered to be closely related to the magnetic helicity. The process of helicity injection by sunspot rotations is summarized in fig. 1.8. Tian & Alexander (2006) suggested that rotations of footpoints of a uniformly twisted flux rope show sign preference as the hemispheric rule. Some observational works suggested that sunspot rotation follows this rule (Richardson, 1941). Many theoretical works reproduced rotating sunspot consistent with this picture (Sturrock et al., 2015; Sturrock & Hood, 2016; Toriumi & Takasao, 2017) as summarized in fig. 1.9. However, some observations argued that the observed sunspot rotational rate does not necessarily follow the hemispheric

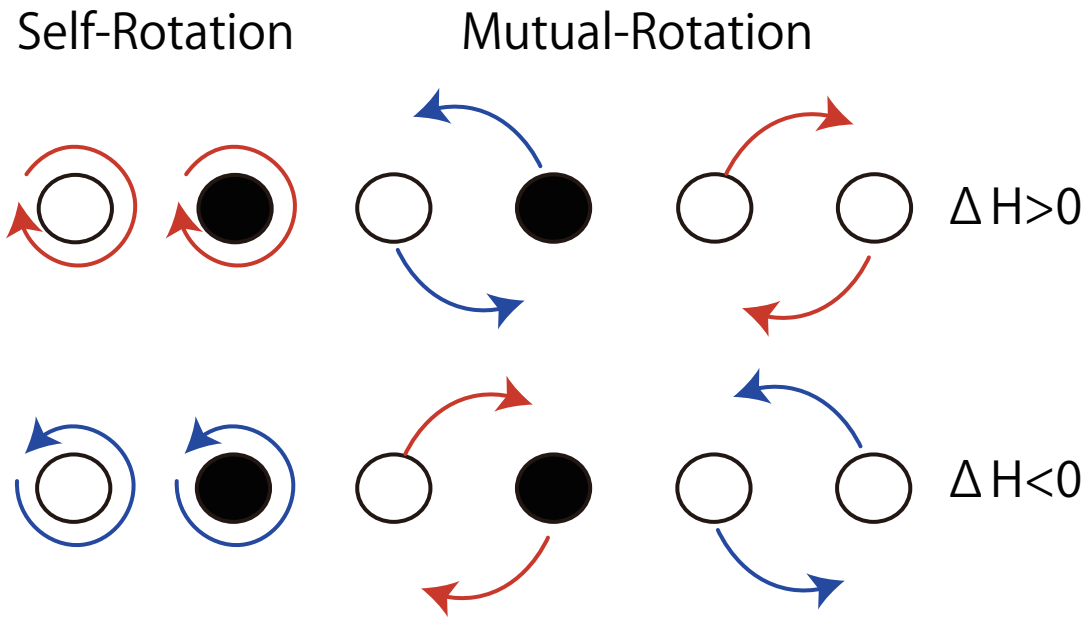

Figure 1.8: Schematics of helicity injection by sunspot rotation. A white (black) circle stands for a positive (negative) polarity sunspot. Red and blue arrows stand for rotational direction of clockwise and counter-clockwise.

rule (Knoska, 1975; Zheng et al., 2016).

1.4 The Role of Opposite Helicity Injection

Recent observational and theoretical studies implied that the helicity injection whose sign is opposite to that of system's global helicity has an important role on the generation of solar flares. Kusano et al. (2003) theoretically proposed the flare trigger model which suggests that the annihilation of positive and negative magnetic helicity triggers solar flares. Park et al. (2012) classified active regions into 2 groups (Group A and B) based on the temporal evolution of magnetic helicity accumulation. In active regions belonging to Group A, magnetic helicity evolution showed simple increasing time profile, and Group B consisted of active regions which showed time profile of sign reversal. They showed that active regions in Group B tended to produce fast CMEs. Park et al. (2013) showed that opposite helicity injection was observed before a large flare occurred. They discussed that the opposite helicity injection reflected the existence of systems having positive and

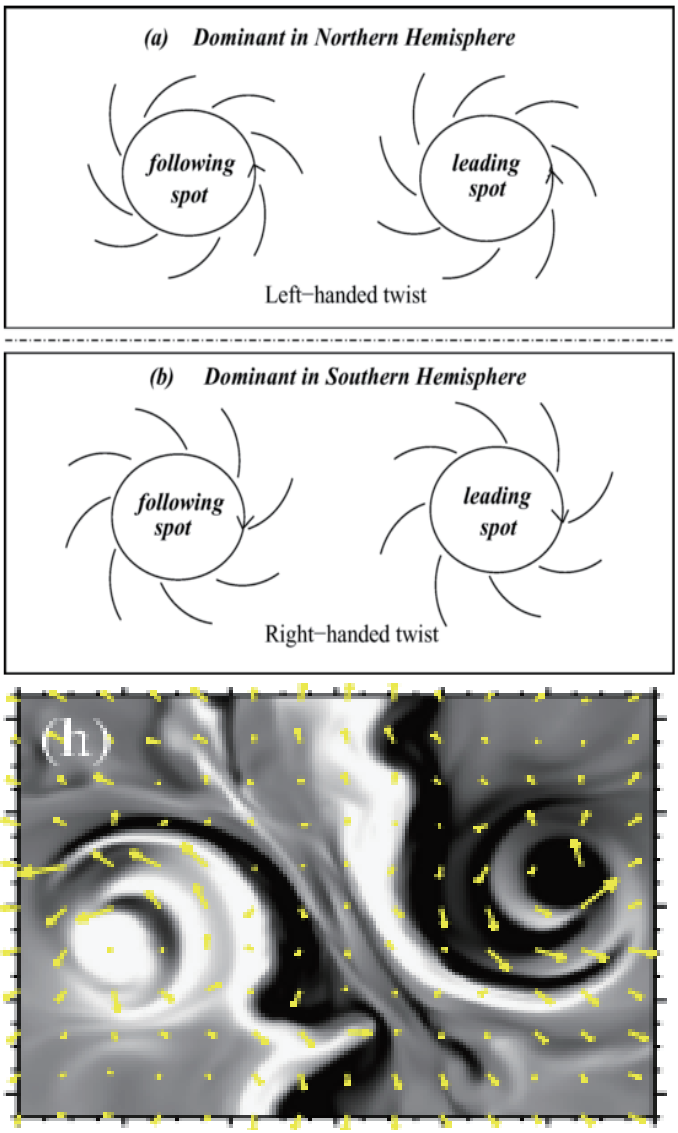

Figure 1.9: (Top, middle) Preferential direction of bipolar sunspot rotation following the hemispheric rule from Tian & Alexander (2006). (Bottom) Numerical simulation shows the rotational motion consistent with the picture from Toriumi & Takasao (2017). Yellow arrows stand for horizontal velocity.

negative helicity and this is a favorable condition for an occurrence of a large flare.

1.5 Purpose of This Thesis

We describe the present knowledge about solar flares in the preceding sections. However, many aspects of solar flares remain unravelled. The following two questions are the most fundamental and important questions.

1. What is the trigger process of solar flares?

2. How, where and when is the free energy for a solar flare stored in coronal magnetic field?

The first question comes from the fact that mere storage of free energy cannot cause solar flares. Therefore, some trigger mechanism is required. Recent studies showed that interactions of systems which have opposite magnetic twist or shear, i.e. helicity, play an important role in causing large flares (Kusano et al. (2012), etc.).

Concerning the second question, free energy can be evaluated using NLFFF extrapolation. However, extrapolated field is strongly affected by a method of modeling, and Schrijver et al. (2008) pointed out that magnetic field extrapolated with some methods does not store efficient free energy for an X-class flare. Therefore, it is challenging to assess the free energy.

Thus, in this thesis, we track the evolution of the coronal energetic state estimating the magnetic helicity injection which can be considered as a robust tracer. To investigate how free energy is stored, and how the sign of helicity is related to occurrences of flares, we identify what kind of motion of magnetic field injects magnetic helicity characteristically. Therefore, the aims of this thesis can be described with the following list of topics;

1. How is magnetic helicity accumulated?

2. Is the opposite helicity injection important for the occurrence of a large solar flare?

3. What features of magnetic field evolution are important for build-up of free energy and flare trigger?

4. What features of magnetic field evolution are attributed to the opposite magnetic helicity injection?

To tackle these questions, we study the magnetic field and magnetic helicity evolution in the active region NOAA 12297 which appeared in March 2015. This active region was very flare-productive generating several M-class flares and an X-class flare. In Chapter 2, we describe the available solar observations we used in the present work. In Chapter 3, we present analysis methods. In Chapter 4, we introduce NOAA 12297 and show results of our analysis. In Chapter 5, we discuss the results. In Chapter 6, we summarize our study.

Chapter 2

Observations

In this chapter, we describe the data and the instrumentation used in this study. We employed data obtained with the Atmospheric Imaging Assembly (AIA; Lemen et al. 2012) and the Helioseismic Magnetic Imager (HMI; Schou et al. 2012) on board the Solar Dynamics Observatory (SDO; Pesnell et al. 2012, fig.2.1), and the Solar Optical Telescope (SOT; Tsuneta et al. 2008; Suematsu et al. 2008; Shimizu et al. 2008; Ichimoto et al. 2008; Lites et al. 2013) on board the $Hinode$ satellite (Kosugi et al. 2007, fig. 2.2). In Section 2.1 and Section 2.2, we describe details of the SDO and the Hinode observations and data processing respectively.

2.1 SDO Observation

The AIA observes the full-disk of the Sun with 7 EUV and 2 UV wavelength channels. Observed channels of wavelength, primary ion(s), observed region and characteristic temperature are summarized in table 2.1. Pixel size is 0".6 and the cadence is 12 seconds for EUV channels and 24 seconds for UV channels.

The HMI instrument obtains full-disk filtergrams with a spatial sampling of 0".5/pix at the 6 narrow bands whose width is 76mÅ centered at the magnetically sensitive 6173Å Fe I photospheric line to measure the Stokes vector (I,Q,U,V). The Stokes parameters reflect

Channels	Primary ion(s)	Region	log(Temperature)
4500Å	continuum	photosphere	3.7
1700Å	continuum	photosphere	3.7
304Å	He II	temperature minimum, photosphere	4.7
1600Å	C IV + cont.	chromosphere, transition region	5.0
171Å	Fe IX	quiet region, upper photosphere	5.8
193Å	Fe XII, XXIV	corona and hot flare plasma	6.2, 7.3
211Å	Fe XIV	active region corona	6.3
335Å	Fe XVI	active region corona	6.4
94Å	Fe XVIII	flaring corona	6.8
131Å	Fe VIII, XXI	transition region, flaring corona	5.6, 7.0

Table 2.1: AIA observation details.

the full polarization state of the electromagnetic field and are defined as

$$I = \kappa(\langle E_x^2 \rangle + \langle E_y^2 \rangle) \tag{2.1}$$

$$Q = \kappa(\langle E_x^2 \rangle - \langle E_y^2 \rangle) \tag{2.2}$$

$$U = 2\kappa(E_x E_y \cos(\phi(t))) \tag{2.3}$$

$$V = 2\kappa(E_x E_y \sin(\phi(t))) \tag{2.4}$$

where E_x and E_y stand for x- and y-component of electromagnetic waves, $\phi(t)$ is the phase of the waves and κ is a dimensional constant to translate the Stokes parameters into the unit of intensity. The Stokes parameter I represents intensity, Q the difference of intensity of linear polarization components between 0° and 90°, U the difference of intensity of linear polarization components between 45° and 135°, and V the difference of intensity of circular polarization components.

Since magnetic field changes the polarization state of the light by the Zeeman effect, photospheric magnetic field vector can be inferred with the Stokes vector. In the case of HMI data, the Stokes vector is calibrated with the HMI science data processing pipeline while the magnetic field vector is derived with the Very Fast Inversion of the Stokes Vector algorithm (Borrero et al., 2011) based on the Milne-Eddington atmospheric model in which the medium is uniform along the optical depth and source function vector depends

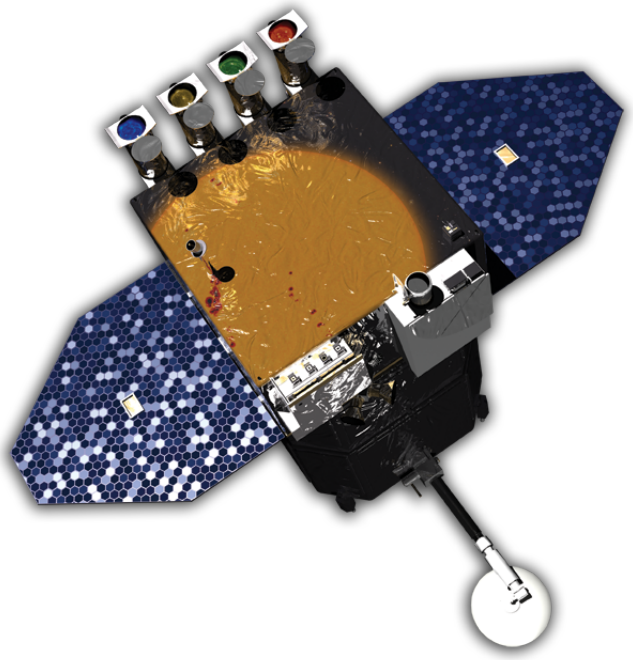

Figure 2.1: The SDO satellite.

linearly on the optical depth. The 180 degrees ambiguity of the azimuthal component is solved with the Minimum Energy Method (Metcalf, 1994; Metcalf et al., 1995; Leka et al., 2009) which determines the azimuthal angle by minimizing a functional containing electric current and the divergence of magnetic field. The Solarsoft routine AIA_PREP is applied to the AIA and HMI data for calibration and co-alignment.

In this thesis, we also use the HMI SHARP CEA data set. This data set is with 12-minute cadence and magnetic field vector is projected into the local solar coordinate with Lambert cylindrical equal area projection (Calabretta & Greisen, 2002; Sun, 2013) from direct cutout of the full disk HMI image in the native coordinate reference system.

2.2 *Hinode* Observation

We also used the magnetic field data obtained by the Spectro-Polarimeter (SP) installed in the SOT on board the *Hinode* satellite. The SP measures with high spectral sampling of 21.6mÅ the four Stokes parameters (I,Q,U,V) of two magnetically sensitive Fe I lines

Figure 2.2: The $Hinode$ satellite.

at 6301.5Å and 6302.5Å with the Polarization Modular Unit (PMU). The calibration of Stokes parameters is performed with the Solarsoft routine SP_PREP (Lites & Ichimoto, 2013). Fitting the observed Stokes parameters, we infer the field strength, inclination and azimuthal angle (and other physical parameters) with the inversion code MEKSY (developed by Dr. T. Yokoyama). The model atmosphere is assumed, as in the case of SDO/HMI, as the Milne-Eddington atmosphere. Moreover, 180 degrees azimuthal ambiguity is also solved with the Minimum Energy Method.

Chapter 3

Analysis Method

In this chapter, we describe the method employed to analyze the magnetic field in NOAA 12297. We estimate the physical parameters associated with non-potentiality of magnetic field described in Section 3.1. We describe about the optical flow method "DAVE" used to derive the footpoint velocity field in Section 3.2. Finally, we describe about the NLFFF extrapolation method in Section 3.3.

3.1 Analysis of Magnetic Field and Helicity Evolution

In order to characterize the evolution of this active region, we derive the physical parameters associated with the complexity of magnetic field.

Magnetic Helicity Accumulation and Helicity Flux Density

We investigate the spatial distribution of the magnetic helicity injection. To derive physically meaningful helicity injection maps, we calculate G_θ described in Section 1.2.2. Magnetic helicity accumulation ΔH is defined as the spatial and temporal integration of G_θ,

$$\Delta H(t) = \int_{t_0}^{t} \int_{S_p} G_\theta dS dt. \tag{3.1}$$

Spinning and Braiding Helicity Injection

The origin of the magnetic helicity injection at the photosphere can be divided into two different contributions of spinning and braiding motions. Spinning and braiding helicity injection correspond to contribution by self and mutual rotations of magnetic patches (as shown in fig. 1.8), respectively. Longcope et al. (2007) proposed the definition of spinning and braiding helicity injection as

$$\dot{H}_{spin} = -2\sum_a \int_{S_a} (\mathbf{A}^{\mathbf{a}}_{\mathbf{P}} \cdot \mathbf{u}) B_z dS_a \tag{3.2}$$

$$\dot{H}_{braid} = -\frac{1}{\pi}\sum_a \sum_{b\neq a} \int_{S_a \ni \mathbf{x}} \int_{S_b \ni \mathbf{x}'} \frac{\hat{\mathbf{z}} \times (\mathbf{x}-\mathbf{x}') \cdot \mathbf{u}(\mathbf{x})}{r^2} B_z(\mathbf{x}) B'_z(\mathbf{x}') dS_b dS_a \tag{3.3}$$

$$\frac{dH}{dt} = \dot{H}_{spin} + \dot{H}_{braid} \tag{3.4}$$

where r is the distance between **x** and **x'**, $\mathbf{A}^{\mathbf{a}}_{\mathbf{P}}$ is the decomposed vector potential of the potential magnetic field, contributed by the region "a", and formulated by a Green's function

$$\mathbf{A}^{\mathbf{a}}_{\mathbf{P}}(\mathbf{x}) = \frac{1}{2\pi} \int_{S_a} \frac{\hat{\mathbf{z}} \times (\mathbf{x}-\mathbf{x}')}{r^2} B'_z(\mathbf{x}') dS_a, \tag{3.5}$$

and full vector potential is

$$\mathbf{A}_{\mathbf{P}}(\mathbf{x}) = \sum_a \mathbf{A}^{\mathbf{a}}_{\mathbf{P}}(\mathbf{x}). \tag{3.6}$$

As shown in Chapter 4, we focus on the self rotation of a spot and mutual rotation between a spot and regions that harbor an emerging flux. To quantify the contribution of these rotational motions, we define the spinning helicity injection by a given magnetic patch "a" as

$$\dot{H}^a_{spin} = -2 \int_{S_a} (\mathbf{A}^{\mathbf{a}}_{\mathbf{P}} \cdot \mathbf{u}) B_z dS_a \tag{3.7}$$

and braiding helicity injection by given magnetic patches "a" and "b" as

$$\dot{H}^{ab}_{braid} = -\frac{1}{\pi}\Big[\int_{S_a \ni \mathbf{x}} \int_{S_b \ni \mathbf{x}'} \frac{\hat{\mathbf{z}} \times (\mathbf{x} - \mathbf{x}') \cdot \mathbf{u}(\mathbf{x})}{r^2} B_z(\mathbf{x}) B'_z(\mathbf{x}') dS_b dS_a \tag{3.8}$$

$$+ \int_{S_b \ni \mathbf{x}} \int_{S_a \ni \mathbf{x}'} \frac{\hat{\mathbf{z}} \times (\mathbf{x} - \mathbf{x}') \cdot \mathbf{u}(\mathbf{x})}{r^2} B_z(\mathbf{x}) B'_z(\mathbf{x}') dS_a dS_b \Big]. \tag{3.9}$$

The label "a" stands for a spot and "b" stands for areas of an emerging flux.

Mean Angular Rotation

We evaluate the rotational rate of the whole body of a spot using the "mean angular rotation" (Longcope et al., 2007) defined as

$$\omega_a = -\frac{2\pi \dot{H}^a_{spin}}{\Phi_a^2} \tag{3.10}$$

where Φ_a stands for total magnetic fluxes in the patch "a"

$$\Phi_a = \int_{S_a} B_z(\mathbf{x}) dS_a. \tag{3.11}$$

The Average Force-Free Alpha: α_{av}

To evaluate the complexity of the horizontal component of the magnetic field, we calculate α_{av} which is an averaged value of the force-free α described in Eq. (1.5) in a spot. This parameter is the index of twist of the magnetic field in a sunspot and is related to the current helicity. As shown in Eq. (1.5), this value is basically the ratio of vertical electric current to vertical magnetic field. There are some methods to define α_{av} (Hagino & Sakurai, 2004). In this thesis, we use the following definition

$$\alpha^a_{av} = \frac{\int_{S_a} J_z \cdot Sign(B_z) dS_a}{\int_{S_a} |B_z| dS_a}, \tag{3.12}$$

namely, the ratio of integrated vertical electric current to integrated vertical magnetic field in the sunspot.

3.2 Plasma Flow Velocity

In order to calculate the physical parameters described above, not only the photospheric magnetic field but also the footpoint velocity field at the photosphere $\mathbf{u}$ should be computed. In this regard, the velocity field can be derived with the optical flow method. In this study, we derive $\mathbf{u}$ with the algorithm "Differential Affine Velocity Estimator" (DAVE, Schuck (2006)).

We consider the Lagrangian trajectory $\mathbf{R}$ of a fluid element in a time-invariant non-uniform flow. $\mathbf{R}(t; \mathbf{x}_i, t_i)$ represents the location of the fluid element at t, whose position was $\mathbf{x}_i$ at t_i. Consequently, $\mathbf{R}$ satisfies the relation

$$\frac{\partial \mathbf{R}(t; \mathbf{x}_i, t_i)}{\partial t} = \mathbf{v}[\mathbf{R}(t; \mathbf{x}_i, t_i)] \tag{3.13}$$

$$\mathbf{R}(t_i; \mathbf{x}_i, t_i) = \mathbf{x}_i. \tag{3.14}$$

The backward-in-time trajectory is constant;

$$\mathbf{R}(t_i; \mathbf{R}(t; \mathbf{x}_i, t_i), t) = \mathbf{x}_i. \tag{3.15}$$

As a result,

$$\frac{D\mathbf{R}(t_i; \mathbf{x}, t)}{Dt} = \frac{\partial \mathbf{R}(t_i; \mathbf{x}, t)}{\partial t} + \mathbf{J}(t_i; \mathbf{x}, t) \cdot \mathbf{v}(\mathbf{x}) = 0 \tag{3.16}$$

where

$$\mathbf{J}(t_i; \mathbf{x}, t) \equiv \nabla \mathbf{R}(t_i; \mathbf{x}, t) \tag{3.17}$$

is the Jacobian describing the transformation of coordinates from $\mathbf{x}$ to $\mathbf{x}_i$. The exact solution of the continuity equation has the form

$$I(\mathbf{x}, t) = \frac{I[\mathbf{R}(t_i; \mathbf{x}, t), t_i]}{det[\mathbf{J}^{-1}(t_i; \mathbf{x}, t)]} \tag{3.18}$$

where I stands for the intensity and $det[\mathbf{J}^{-1}(t_i; \mathbf{x}, t)]$ is the contraction factor and represents the effect of the divergence and convergence of the Lagrangian trajectory on the mentioned intensity.

Then we minimize a localized "sum of squared difference" correlation integral C_{SSD} with the variational principle;

$$C_{SSD} = \int dtd^2xw(\mathbf{x} - \chi, t - \tau)\{I(\mathbf{x}, t + \Delta t) - \frac{I(R(t; \mathbf{x}, t + \Delta t), t)}{det[\mathbf{J}^{-1}(t; \mathbf{x}, t + \Delta t)]}\}^2 \tag{3.19}$$

where $w(\mathbf{x} - \chi)$ is the apodizing window function to make the analysis localized around χ.

To incorporate not only the advection but also the contraction, dilation, and rotation of a flow, we consider an affine velocity profile;

$$\mathbf{u}_\chi = (U_0, V_0) + \mathbf{W}(\mathbf{P}) \cdot (\mathbf{x} - \chi) \tag{3.20}$$

where

$$\mathbf{W}(\mathbf{P}) = \nabla \mathbf{u}(\mathbf{x})|_{\mathbf{x}=\chi} = \begin{bmatrix} U_x & U_y \\ V_x & V_y \end{bmatrix} \tag{3.21}$$

is the tensor describing the local shear flow. Time difference of Lagrangian trajectory is

$$\frac{\partial \mathbf{R}_\chi(t; \mathbf{x}_i, t_i)}{\partial t} = (U_0, V_0) + \mathbf{W}(\mathbf{P}) \cdot (\mathbf{R}_\chi(t; \mathbf{x}_i, t_i) - \chi) \tag{3.22}$$

where $\mathbf{R}_\chi$ is the Lagrange trajectory which is valid only within the neighborhood of χ.

The valid range is determined by the apodizing window function. Considering the exact solution of this linear system (Schuck, 2005), Eq. (3.19) can be rewritten as

$$C_{SSD} = \int dtd^2xw(\mathbf{x}-\chi, t-\tau)\{I(\mathbf{x}, t+\Delta t) - e^{-(U_x+V_y)\Delta t} I(R_\chi(t;\mathbf{x}, t+\Delta t), t)\}^2. \quad (3.23)$$

The lowest order of the approximation of Eq. (3.23) with the least-square (LS) approach is

$$\begin{aligned} C_{SSD}^{LS} &= \Delta t^2 \int dtd^2xw(\mathbf{x}-\chi, t-\tau)\{\frac{\partial I(\mathbf{x},t)}{\partial t} + \nabla\cdot[I(\mathbf{x},t)\mathbf{u}_\chi(\mathbf{P};\mathbf{x})]\}^2 & (3.24)\\ &= \Delta t^2 \int dtd^2xw(\mathbf{x}-\chi, t-\tau)\{(\frac{\partial I(\mathbf{x},t)}{\partial t})^2 + 2\mathbf{P}\cdot\mathbf{b} + \mathbf{P}\cdot\mathbf{A}\cdot\mathbf{P}\} & (3.25)\end{aligned}$$

where $\mathbf{P} = (U_0, V_0, U_x, V_y, U_y, V_x)$,

$$\mathbf{A} = \begin{bmatrix} G_{xx} & \cdot & \cdot & \cdot & \cdot & \cdot \\ G_{xy} & G_{yy} & \cdot & \cdot & \cdot & \cdot \\ G_x + x'G_{xx} & G_y + x'G_{xy} & G + 2x'G_x + x'^2G_{xx} & \cdot & \cdot & \cdot \\ G_x + y'G_{xy} & G_y + y'G_{yy} & G + x'G_x + y'G_y + x'y'G_{xy} & G + 2y'G_y + y'^2G_{yy} & \cdot & \cdot \\ y'G_{xx} & y'G_{xy} & y'G_x + x'y'G_{xx} & y'G_x + y'^2G_{xy} & y'^2G_{xx} & \cdot \\ x'G_{xy} & x'G_{yy} & x'G_y + x'^2G_{xy} & x'G_y + x'y'G_{yy} & x'y'G_{xy} & x'^2G_{yy} \end{bmatrix} \quad (3.26)$$

is a real symmetric semidefinite structure tensor,

$$\begin{aligned} \mathbf{b} &= (G_{tx}, G_{ty}, G_t + x'G_{tx}, G_t + y'G_{ty}, y'G_{tx}, x'G_{ty})^T & (3.27)\\ G_{ij} &= \frac{\partial I}{\partial x_i}\frac{\partial I}{\partial x_j} & (3.28)\\ G_{ti} &= \frac{\partial I}{\partial t}\frac{\partial I}{\partial x_i} & (3.29)\\ G_i &= I\frac{\partial I}{\partial x_i} & (3.30)\\ G_t &= I\frac{\partial I}{\partial t} & (3.31)\\ G &= I^2, & (3.32)\end{aligned}$$

and

$$\mathbf{x}' = \mathbf{x} - \chi. \tag{3.33}$$

Since

$$\frac{\partial C_{SSD}^{LS}}{\partial \mathbf{P}} = 2\Delta t^2 \int dt d^2x w(\mathbf{x} - \chi, t - \tau)\{\mathbf{b} + \mathbf{P} \cdot \mathbf{A}\} = 0, \tag{3.34}$$

Eq. (3.34) has the Euler-Lagrange equation

$$\langle \mathbf{A} \rangle \cdot \mathbf{P} = -\langle \mathbf{b} \rangle \tag{3.35}$$

where $\langle\rangle$ indicating averaging over the window, $\int dt d^2x w$. Since $\mathbf{A}$ is real symmetric semidefinite structure matrix, $\mathbf{P}$ can be obtained performing the singular value decomposition method. The method 'DAVE' solves the above equations and compute footpoint velocity field.

In this study, we apply the DAVE algorithm to the line-of-sight (LOS) magnetic field obtained by the HMI and compute footpoint velocity field, with the code developed by Dr. P. W. Schuck. We used an apodizing window of 5" (10 pixels) and the magnetic field whose absolute value is less than 50[G] is neglected.

3.3 NLFFF Modeling

For the modeling of the 3-dimensional coronal magnetic field, we perform a nonlinear force-free field (NLFFF) extrapolation with photospheric magnetic field obtained by $Hinode$ SOT/SP. We used the code developed by Inoue et al. (2014) based on the MHD (magneto-hydro dynamics) relaxation method. In this method, first of all, we calculate the 3-dimensional potential field with the Green's function method (Schumidt, 1964) from the normal component of the magnetic field vector B_z at the photosphere, which is obtained

with the $Hinode$ SOT/SP observation. Then we calculate the 3-dimensional magnetic field evolution with the MHD equations neglecting the gas pressure and gravity (force-free condition);

$$\frac{\partial \mathbf{v}}{\partial t} = -(\mathbf{v}\cdot\nabla)\mathbf{v} + \frac{1}{\rho}\mathbf{J}\times\mathbf{B} + \nu\nabla^2\mathbf{v} \tag{3.36}$$

$$\frac{\partial \mathbf{B}}{\partial t} = \nabla\times(\mathbf{v}\times\mathbf{B} - \eta\mathbf{J}) - \nabla\phi \tag{3.37}$$

$$\mathbf{J} = \nabla\times\mathbf{B} \tag{3.38}$$

$$\frac{\partial \phi}{\partial t} + c_h^2\nabla\cdot\mathbf{B} = -\frac{c_h^2}{c_p^2}\phi \tag{3.39}$$

where ρ is the pseudo density, ν is the non-dimensional viscosity set to 1.0×10^{-3}, and ϕ is the convenient potential. ρ is supposed to be proportional to $|\mathbf{B}|$ in order to set the Alfvén speed uniform in space and to make the relaxation of magnetic field easier. The fourth equation plays a role on avoiding the deviation from $\nabla\cdot\mathbf{B} = 0$, introduced by Dedner et al. (2002). c_h and c_p are the advection and diffusion coefficients of $\nabla\cdot\mathbf{B}$. The non-dimensional resistivity η is defined as

$$\eta = \eta_0 + \eta_1\frac{|\mathbf{J}\times\mathbf{B}||\mathbf{v}|^2}{|\mathbf{B}|^2} \tag{3.40}$$

where $\eta_0 = 5.0\times10^{-5}$ and $\eta_1 = 1.0\times10^{-3}$.

To avoid to be affected by the Courant-Friedrichs-Lewy condition, we define $v^* = |\mathbf{v}|/|\mathbf{v}_A|$ where $\mathbf{v}_A$ is the Alfvén speed, and if v^* becomes larger than v_{max}, we modify the velocity $\mathbf{v}$ as

$$\mathbf{v} \rightarrow \frac{v_{max}}{v^*}\mathbf{v}. \tag{3.41}$$

v_{max} is set to 0.01.

We gradually change the transverse component of magnetic field at the bottom bound-

ary $\mathbf{B}_{BC}$ as

$$\mathbf{B}_{BC} = \gamma \mathbf{B}_{obs} + (1 - \gamma)\mathbf{B}_{pot} \tag{3.42}$$

where $\mathbf{B}_{obs}$ and $\mathbf{B}_{pot}$ are the transverse components of the observed and potential magnetic field. γ is a coefficient ranging from 0 to 1. During an iteration, we calculate $\mathbf{R} = \int |\mathbf{J} \times \mathbf{B}| dV$ and, when $\mathbf{R}$ gets lower than a critical value, we increase γ in accordance with $\gamma = \gamma + d\gamma$. $d\gamma$ is set to 0.02. When γ is 1, $\mathbf{B}_{BC}$ is the same as the observed magnetic field. The magnetic field at the top and side boundaries and the normal magnetic field at the bottom boundary are fixed.

We carried out the numerical computation on Supercomputer for earth Observation, Rockets and Aeronautics (SORA) of JAXA. Regarding the numerical methods, the spatial difference is approximated by the second-order central finite difference, and the time integration is by Runge-Kutta-Gill method to fourth-order accuracy. The numerical domain is set to $(0, 0, 0) < (x, y, x) < (1.0, 1.0, 0.5)$ resolved by $(516, 516, 258)$ nodes.

Chapter 4

Results

In this chapter, we describe the results of our analysis. We focus on the active region NOAA 12297 which appeared from the east limb at the beginning of March in 2015. Since this active region produced many large flares close to solar disc center, it is suitable for our flare study. We introduce this active region in Section 4.1. NOAA 12297 had 2 flaring regions. In this study, these regions are labelled as Region 1 and Region 2. They showed different patterns of flare occurrences. However, they had similar configuration of photospheric magnetic field. The details are described in Section 4.2. Focusing on this similarity, we analyze magnetic field and magnetic helicity evolution in both regions. We present the results of Region 1 in Section 4.3 and Region 2 in Section 4.4.

4.1 NOAA 12297

Fig. 4.1 shows the full-disk soft X-ray fluxes from 2015 March 9th to 15th obtained by GOES. Since there was no flare-productive active region except NOAA 12297 during this period, this plot shows that many M-class flares and one X-class flare were produced in NOAA 12297. Large flares occurred especially from 12UT on March 10th to 12UT on 13th. Since NOAA 12297 was located at S16E13 at 00:30UT on 11th, the magnetic field during this period was observed with high accuracy. Therefore, we focus in this study on the magnetic activity during the mentioned period.

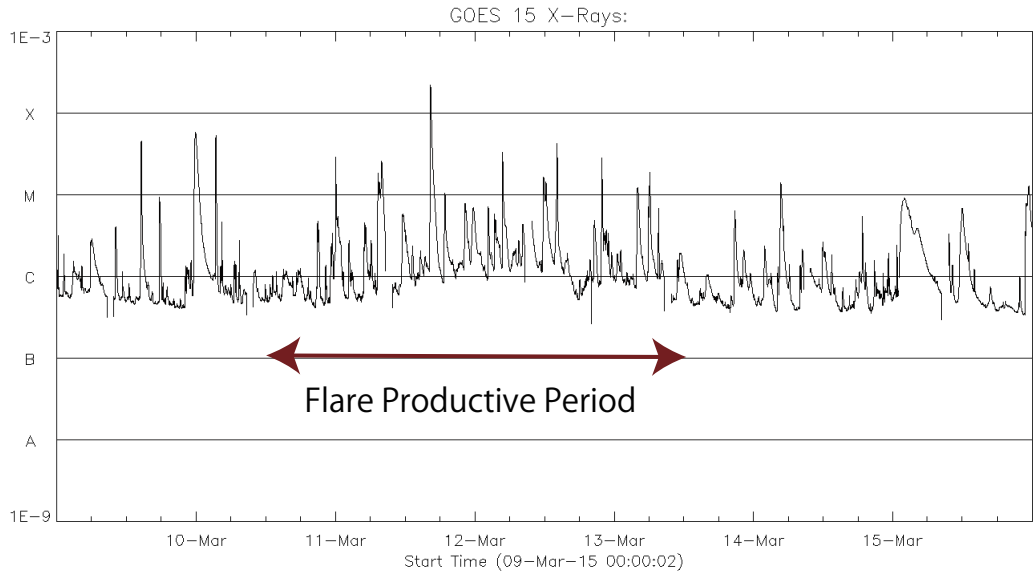

Figure 4.1: The soft X-ray light curve from 0UT on 2015 March 9th to 0UT on 16th. The Sun was very flare-productive from 12 UT on 10th to 12UT on 13th. In this thesis, we focus on the activities during this period.

Fig. 4.2 shows the temporal and spatial magnetic field evolution in the whole region of NOAA 12297. This active region was very complex and mainly composed of a static large sunspot and emerging fluxes. The most prominent magnetic patches are labelled as following; the largest sunspot as P1, scattered negative polarity in the southern region as N1, positive and negative footpoints of an emerging flux at the center of the active region as P2 and N2a, a small negative spot in north-west as N3 and the positive region associated with N3 as P3. The negative elongated magnetic field which emerged in the middle phase is labelled as N2b. Note that, when we mention N2, it means the sum of N2a and N2b.

4.2 Description on Flaring Regions

Symbols in fig. 4.3 correspond to the positions where flares larger than M-class occurred from 12UT on March 10th to 12UT on 13th. White and yellow symbols stand for the locations of M-class and X-class flares, respectively. The positions are determined as centers of gravity of brightening at 1600Å obtained with the AIA, namely, flare ribbons.

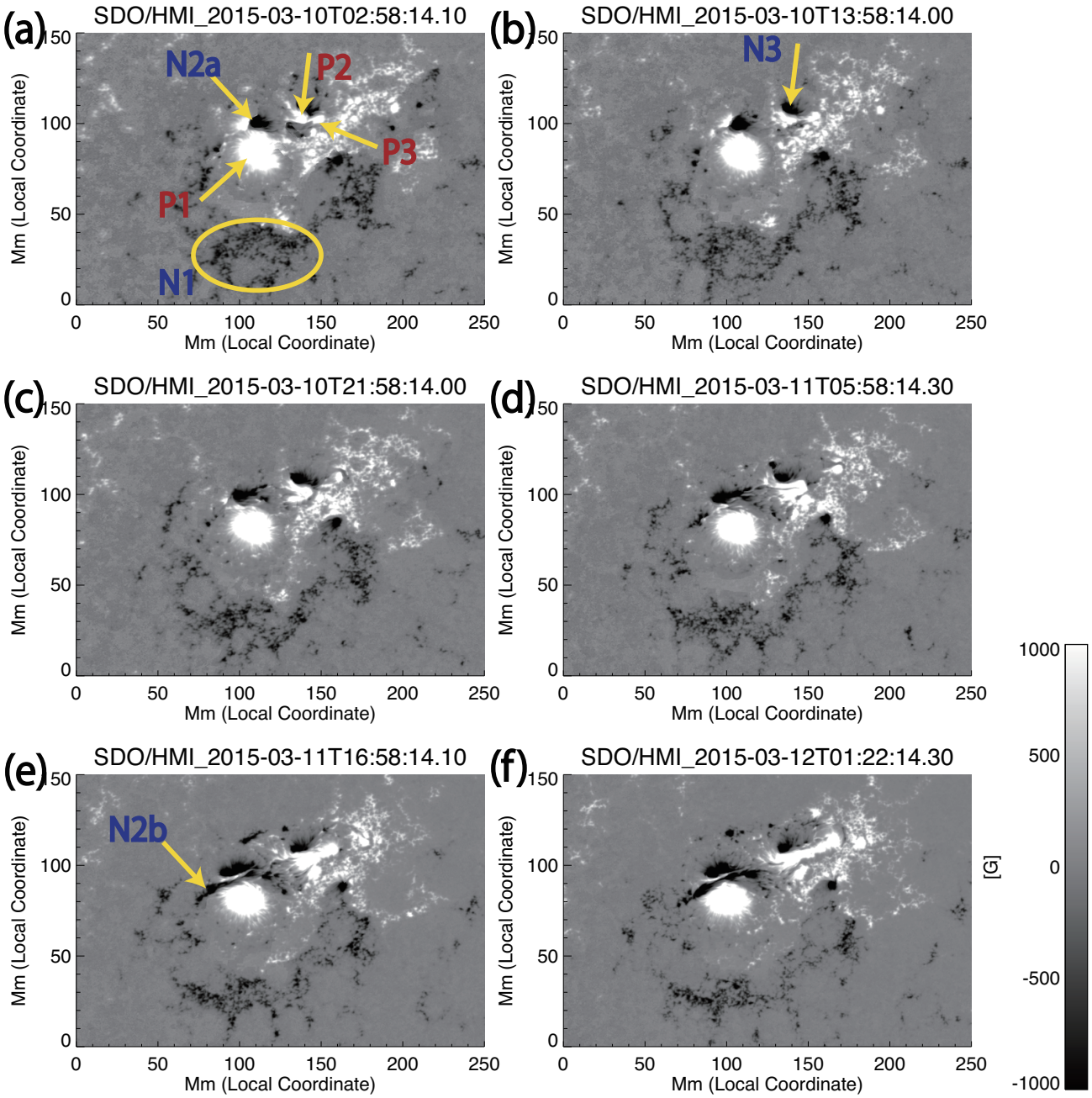

Figure 4.2: Temporal evolution of vertical magnetic field in NOAA 12297. Main magnetic patches are labelled; the largest sunspot as P1, scattered negative polarity in the southern region as N1, positive and negative footpoints of the emerging flux at the center of the active region as P2 and N2a, small negative spot in north-west as N3 and positive region associated with N3 as P3 as shown in (a) and (b). Negative elongated magnetic field which emerged from the timing of (c) is labelled as N2b as shown (e).

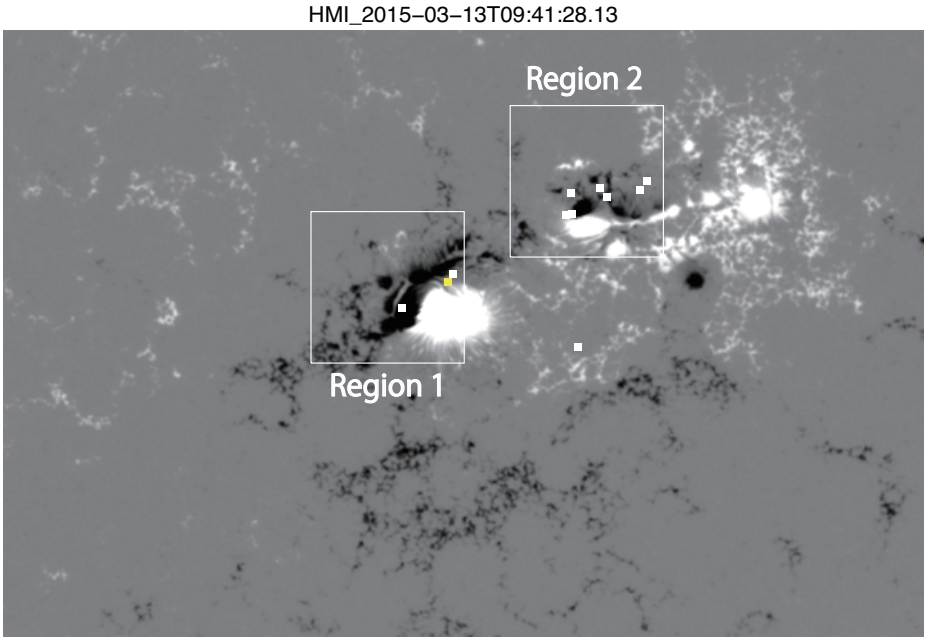

Figure 4.3: Positions where flares larger than M-class occurred are plotted. White and yellow symbols stand for M-class and X-class flares, respectively. The background image is LOS magnetic field at 09:41UT on 13th.

This figure shows that this AR has 2 flaring regions. The eastern region is labelled as Region 1 and the western region as Region 2. Region 1 contains P1 and N2 and Region 2 includes P2 and N3. Fig. 4.4 shows lightcurves of AIA 1600Å. Top plot is the lightcurve in the whole active region, middle is in Region 1 and bottom is in Region2. Magnitude of flares larger than M1.0 are noted. Fig. 4.3 and 4.4 imply that Region 1 and 2 showed difference in frequency and magnitude of flares. In Region 1, the number of flares larger than M-class was only 3 although the largest flare (X2.1) occurred. On the other hand, in Region 2, several flares of M-class occurred (a total of 7 flares). Note that one M1.4 flare occurred in the region except for Region 1 and 2, and one M-class flare could not be observed by the AIA.

Although Region 1 and 2 showed different flaring pattern, both regions displayed a similar magnetic field evolution. One footpoint of an emerging flux moved beside the sunspot. That motion can be considered as mutual rotation of one footpoint of an emerging bipole (N2 in Region 1 and P2 in Region 2) with respect to a spot (P1 in Region 1 and N3 in Region 2) in the counter-clockwise direction. The difference between the two

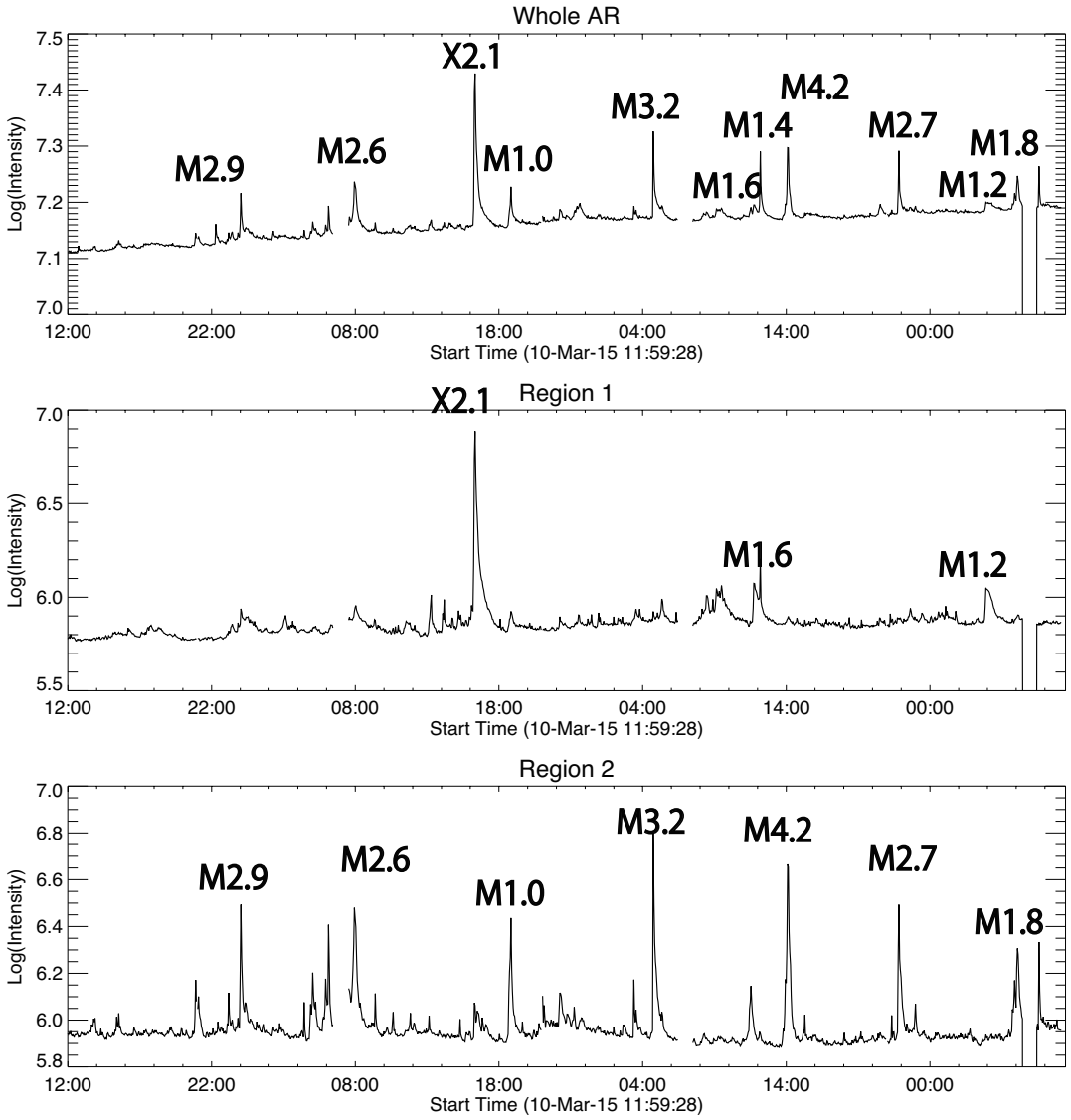

Figure 4.4: AIA 1600Å light curve (a) in the whole AR, (b) in Region 1 and (c) in Region 2.

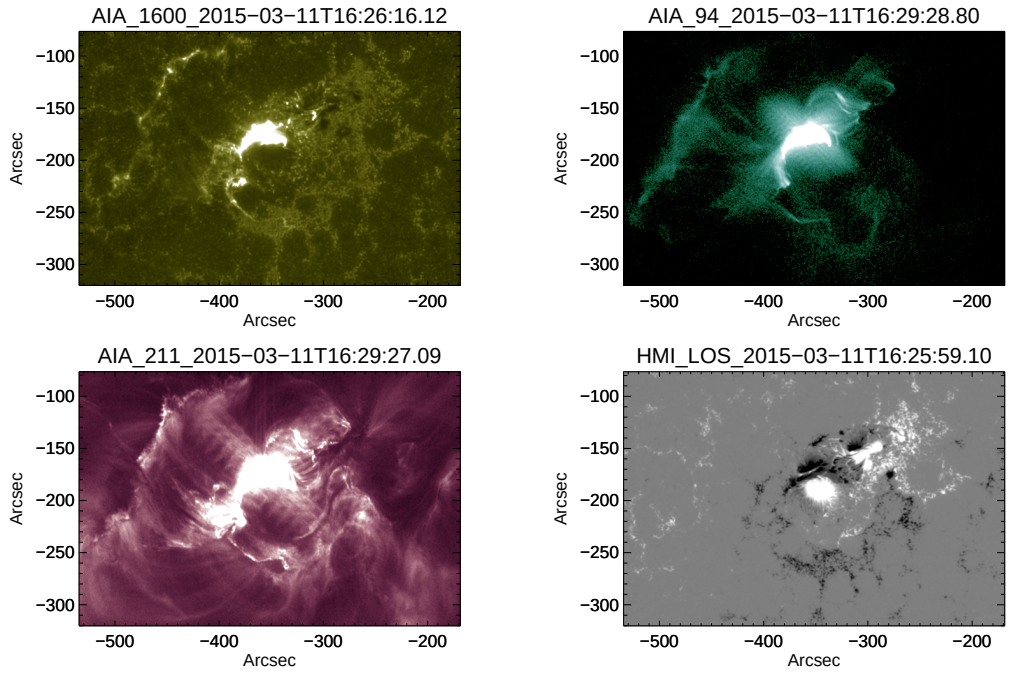

Figure 4.5: EUV images at the time of X2.1 flare taken by the AIA in the wavelength of (Top left) 1600Å, (Top right) 94Å and (Bottom left) 211Å. (Bottom right) The image of LOS magnetic field at the corresponding time.

regions is that P1 is a large and mature sunspot while N3 is a small and young sunspot.

4.3 Region 1 — the X2.1 Flare

4.3.1 Evolution of Magnetic Field, Magnetic Helicity and Associated Parameters

In Region 1, 3 flares larger than M-class occurred. The EUV features in the wavelengths of 1600Å, 94Å, 211Å, and LOS magnetogram at the flare time are shown in fig. 4.5∼4.7. In particular, the largest X2.1 flare, shown in fig. 4.5, occurred at 16:11UT on 11th. The CME was ejected when the flare occurred with helical motion similar to Török & Kliem (2005).

Enlarged maps of vertical magnetic field around the Region 1 are shown in fig. 4.8. Red arrows represent the horizontal component of the magnetic field. In panels (a), (b)

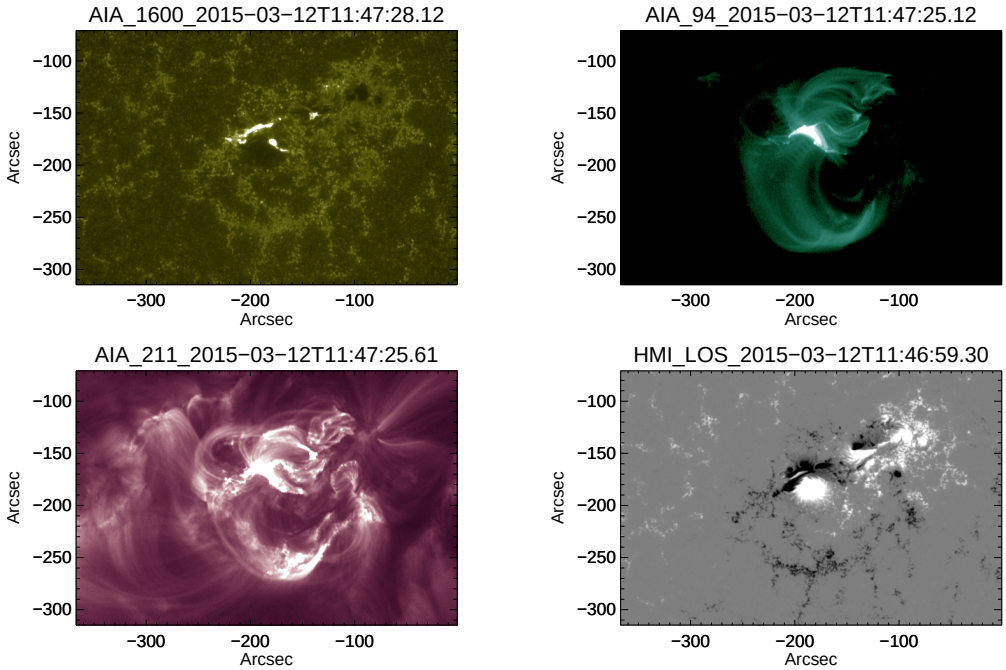

Figure 4.6: EUV images at the time of M1.6 flare taken by the AIA in the wavelength of (Top left) 1600Å, (Top right) 94Å and (Bottom left) 211Å. (Bottom right) The image of LOS magnetic field at the corresponding time.

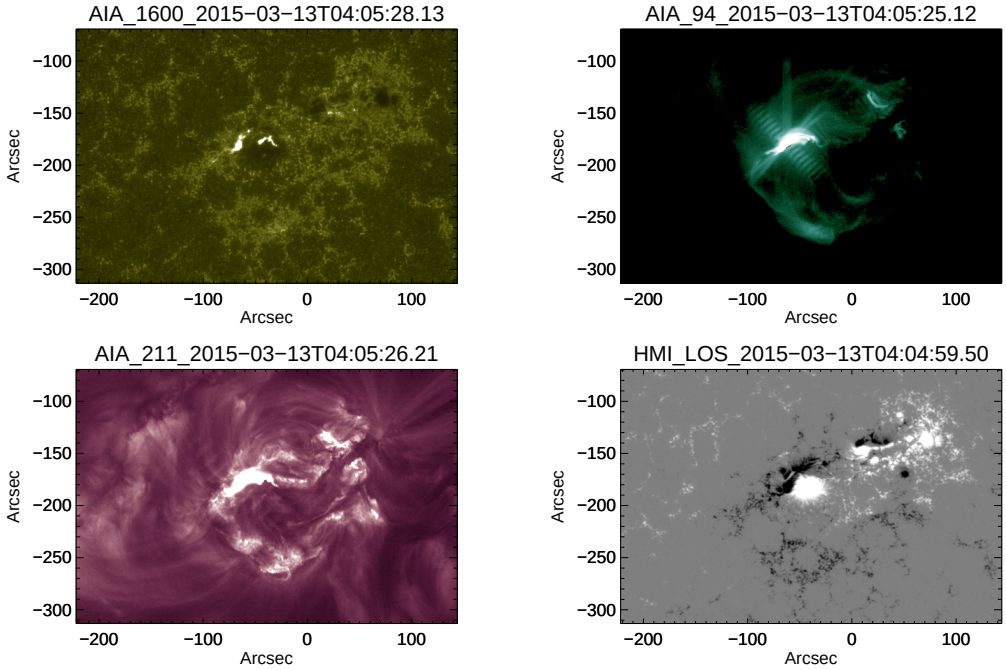

Figure 4.7: EUV images at the time of M1.2 flare taken by the AIA in the wavelength of (Top left) 1600Å, (Top right) 94Å and (Bottom left) 211Å. (Bottom right) The image of LOS magnetic field at the corresponding time.

and (c), N2a showed the eastward proper motion in the north of P1. Soon after the timing of (c), N2b started to emerge between P1 and N2a.

Fig. 4.9 shows enlarged G_θ maps in the Region 1, namely, temporal and spatial helicity flux density. Panels (a), (b) and (c) show that P1 injected positive magnetic helicity. However, (d) and (e) show that, after the emergence of N2b, P1 started to inject negative magnetic helicity. The negative sign is opposite to the sign of the global magnetic helicity. In panel (f), a part of P1 again injected positive magnetic helicity. The emerging flux N2 had positive magnetic helicity in the all panels.

In fig. 4.10, associated physical parameters are summarized; (a) absolute magnetic flux in P1 and (b) N2, (c) mean angular rotation of P1, (d) α_{av} in P1, (e) spinning helicity injection by P1 and (f) braiding helicity injection by P1 and N2. In the numerical calculation, P1 is defined with the B_z threshold of 1000[G] and N2 is defined as the set of pixels having magnitude of B_z less than -1000[G] in the arbitrary box-shaped region. Parameters except for absolute magnetic fluxes (in panels (a) and (b)) are averaged over 1.5 hours.

The magnetic flux in P1 did not increase in the period. Therefore P1 was in the late phase of its evolution. Increase of negative magnetic flux in panel (b) was attributed to the rapid emergence of N2b. If we compare (b) with other parameters, we find that the rotational reversal and the increase of α_{av} occurred in the early phase, and the X-class flare occurred in the middle phase of N2b emergence. With panels (e) and (f), contributions of spinning of P1 and braiding of P1 and N2 can be compared. The average value of spinning and braiding helicity injection from 12UT to 20UT on 11th is $-2.69 \times 10^{37}[Mx^2/s]$ and $1.23 \times 10^{37}[Mx^2/s]$, respectively. Then in this period, the spinning helicity injection is a factor ~ 2 larger than the braiding helicity injection, and spinning helicity injection of opposite sign dominated in Region 1.

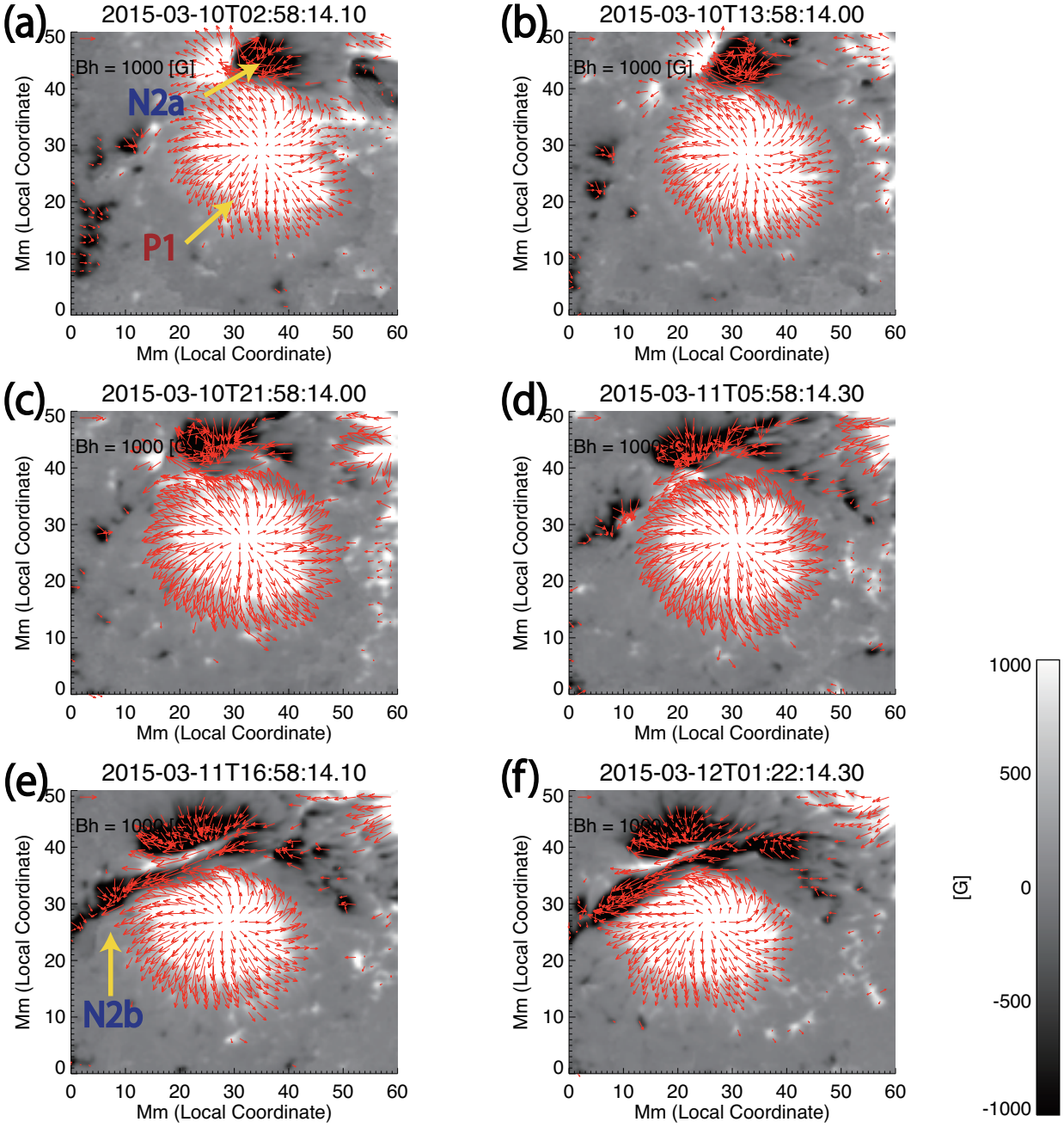

Figure 4.8: B_z maps enlarged in Region 1. The background color maps show vertical magnetic field obtained by HMI. Red arrows represent the horizontal magnetic field.

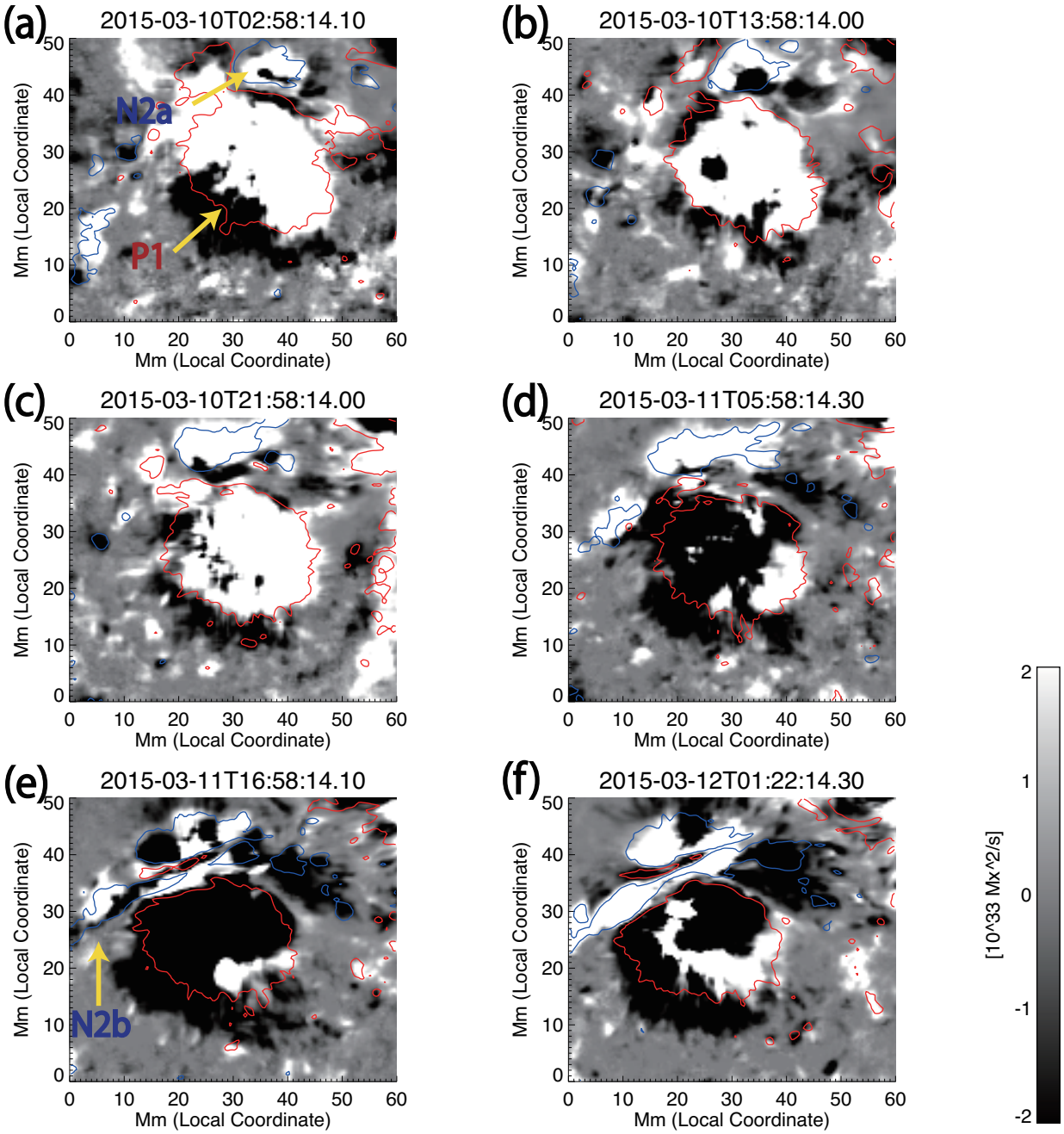

Figure 4.9: G_θ maps enlarged in Region 1. Red and blue contours represent $B_z = \pm 500[G]$.

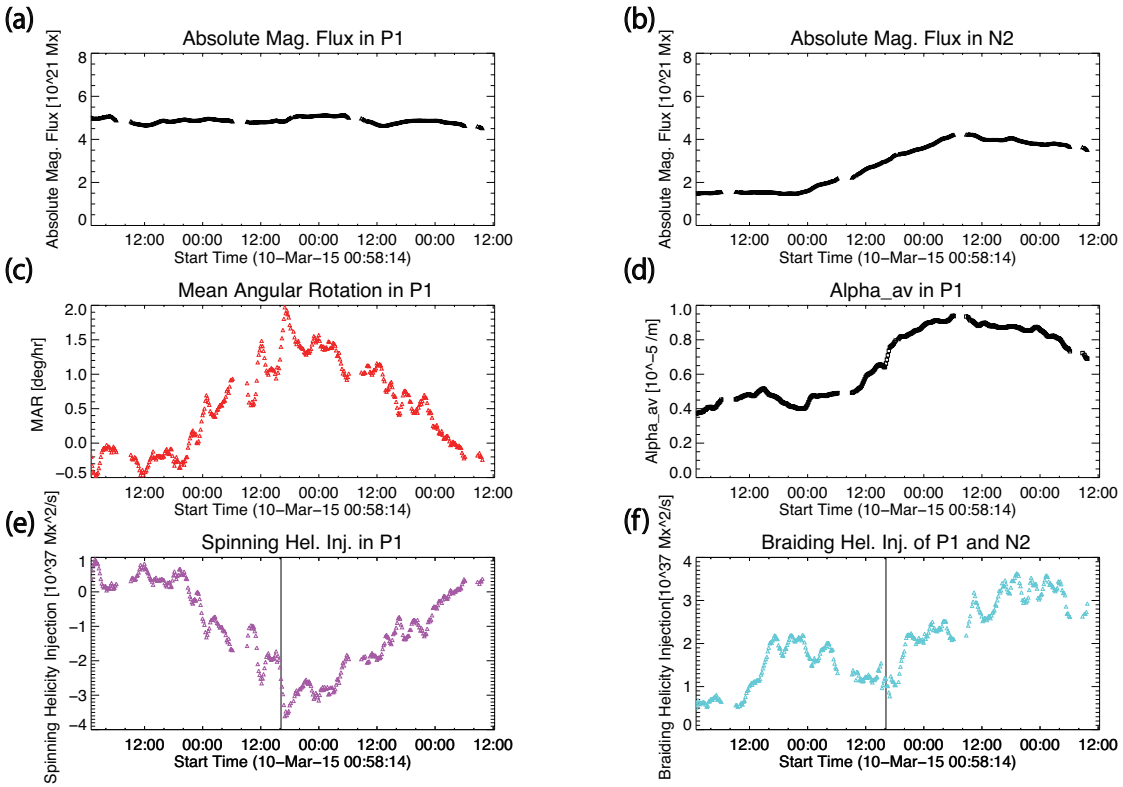

Figure 4.10: Temporal evolution of associated parameters in Region 1. (a) Absolute magnetic flux of a spot (P1), (b) absolute magnetic flux of an emerging flux (N2), (c) mean angular rotation of a spot (P1), (d) α_{av} in a spot (P1), (e) spinning helicity injection in a spot (P1), (f)braiding helicity injection between a spot (P1) and an emerging flux (N2). The vertical solid line in panels (e) and (f) represents the start time of the X2.1 flare.

4.3.2 The Reversed Rotation of the Sunspot P1

After performing the analysis of the magnetic field before and after the X2.1 flare, we find that P1 rotated clockwise in the initial stage, but it started to rotate in the counter-clockwise direction accompanied by the emergence of N2b.

In fig. 4.11, the temporal evolution of the mean angular rotation of the sunspot P1, α_{av} in P1, and the magnetic helicity accumulation in the active region ΔH are plotted in red, black, and blue symbols respectively. When mean angular rotation is calculated, errors are estimated by pseudo Monte Carlo method. Namely, we add the random errors to magnetograms and perform DAVE, then we calculate the parameter with the magnetic field and obtained the velocity field. We repeat this calculation 50 times. Errors are estimated as the standard deviation (1σ) of those results. Added error has the Gaussian distribution and its width (1σ) is 20[G].

Through this period, ΔH and α_{av} were positive. In the first stage of the period, the mean angular rotation rate was positive, hence P1 rotated clockwise. The rate during this period was about $-0.289[deg/hr]$. The rotation of this direction injects positive helicity. Fast flux emergence of N2b started at 22UT on 10th. Accompanied by the emergence, the mean angular rotation rate increased suddenly and became positive. This means P1 started to rotate reversely; counter-clockwise. The greatest value of the rate was about $2.21[deg/hr]$. From the time when P1 started to rotate reversely and to inject negative magnetic helicity, ΔH stopped the monotonic increase. When the X-class flare occurred, ΔH nearly unchanged. ΔH increased monotonicaly again from 19UT on 11th. Although the helicity injection in P1 changed its polarity, the current helicity α_{av} showed a different behavior. After some delay behind the rotational reversal, α_{av} was still positive and suddenly increased. This means that positive current helicity was injected in P1, contrary to what happened with the magnetic helicity injection. The average of α_{av} before 22UT on 10th was about $0.45 \times 10^{-5}[/m]$ and the value at the start time of the flare was about $0.66 \times 10^{-5}[/m]$. Finally, the X2.1 flare occurred at 16:11UT on 11th (the vertical line in

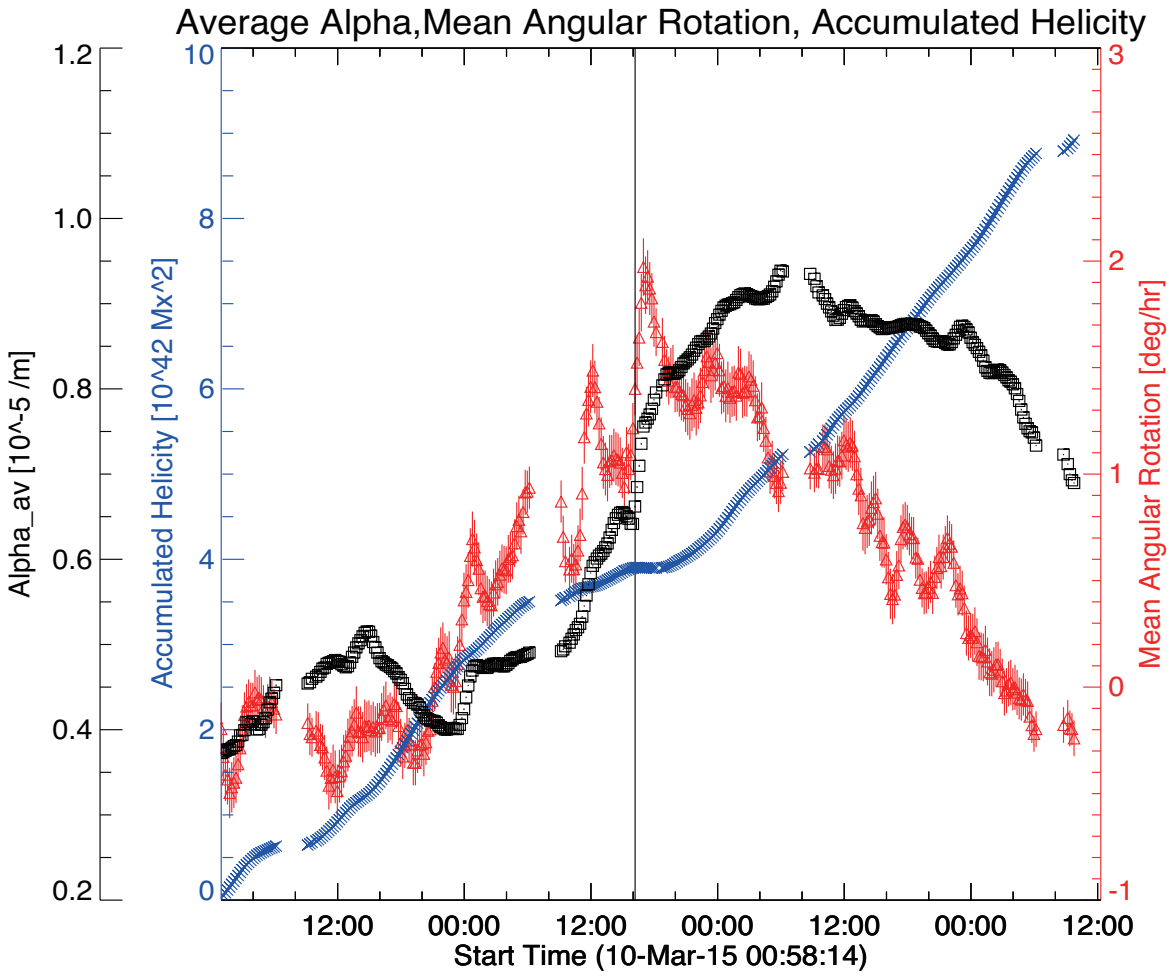

Figure 4.11: Temporal evolution of important parameters. Mean angular rotation(red triangles), α_{av} (black squares) of P1 and accumulated helicity of the whole AR (blue cross) are plotted. The vertical solid line represents the start time of the X2.1 flare.

fig. 4.11). Soon after the flare, the rotation speed of P1 decelerated and became clockwise again on 13th.

Additionally, we confirm the feature of P1's rotation with images of B_z (fig. 4.12). We track vertical magnetic field on pixels shown in fig. 4.12(a) as a red curve. The radius of the circle is 23 pixels(8.4 Mm). To make detection of rotation easy, we mask pixels whose values are negative.

The angle-time plot is shown in fig. 4.12(b). Red and blue arrows represent clockwise and counter-clockwise rotation respectively. This plot shows that before 0UT on 11th P1 rotated clockwise subtly, however after the time, it rotated counter-clockwise. The timing when P1 started to rotate reversely is different from previous results and it may be due to a difference in methods.

4.3.3 Magnetic Connectivity in the Corona

Left column in fig. 4.13 shows vertical magnetic field obtained by the SOT/SP. Middle column in fig. 4.13 shows corresponding 3-dimensional magnetic field reproduced by the NLFFF extrapolation. Before the emergence of N2b, N2a and P1 were connected during N2a emergence and arcade-line magnetic field structure was formed (blue). After N2b emerged, the connectivity between P1 and N2b was newly formed (red). Red magnetic fields were highly sheared at local spatial scales before the X-class flare. Additionally, right column in fig. 4.13 shows AIA 211Å images before and after the onset of the CME. As shown with yellow arrows, the position of sheared red field lines corresponds to the position where the CME was ejected. This CME showed helical motion.

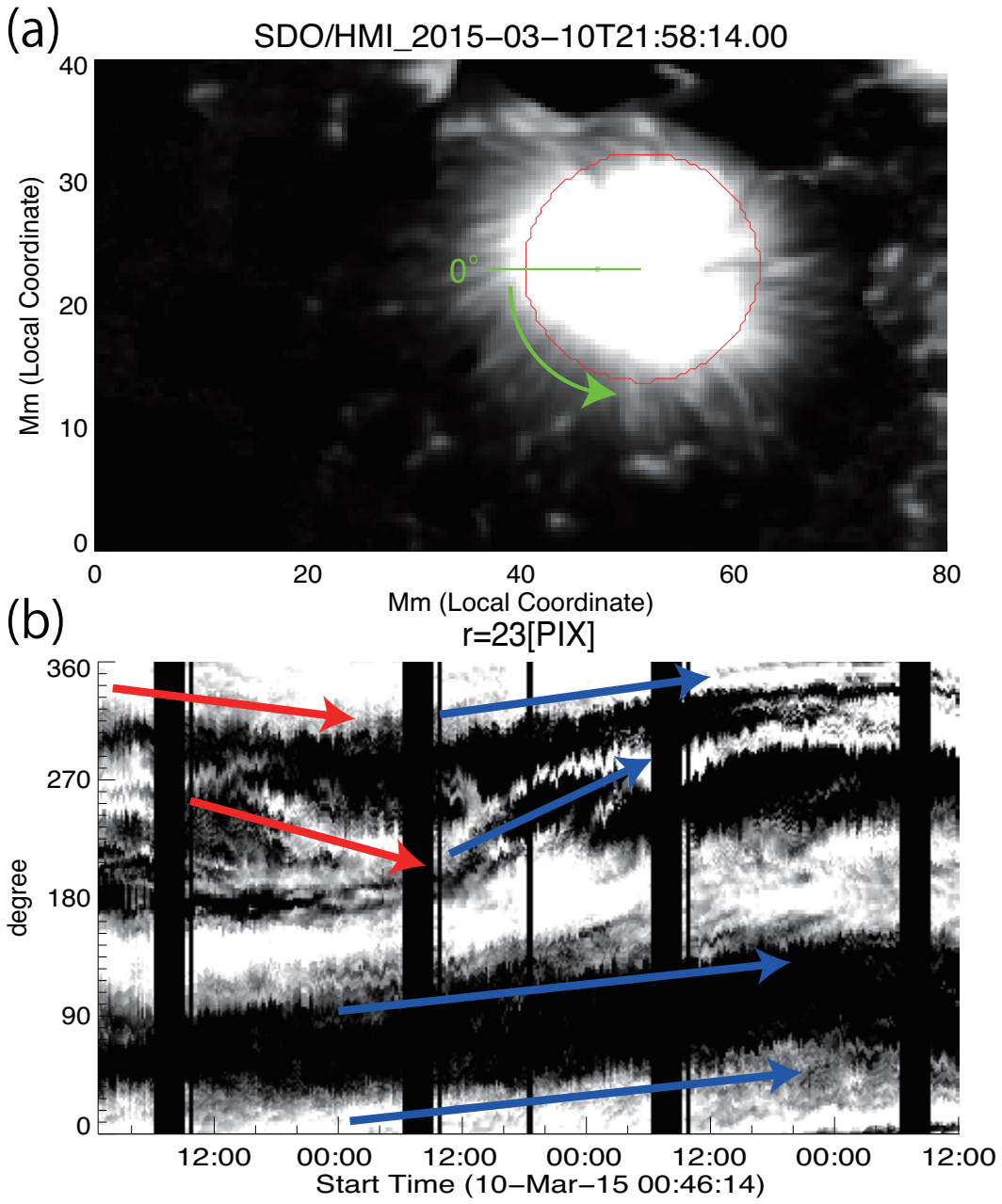

Figure 4.12: (a) A map of B_z at 21:58UT on 10th. Pixels having negative values are masked. Rotation motion of the sunspot is tracked on the red circle whose radius is 23 pixels (8.4 Mm). (b) Angle-time plot. Red and blue arrows represent clockwise and counter-clockwise rotation respectively.

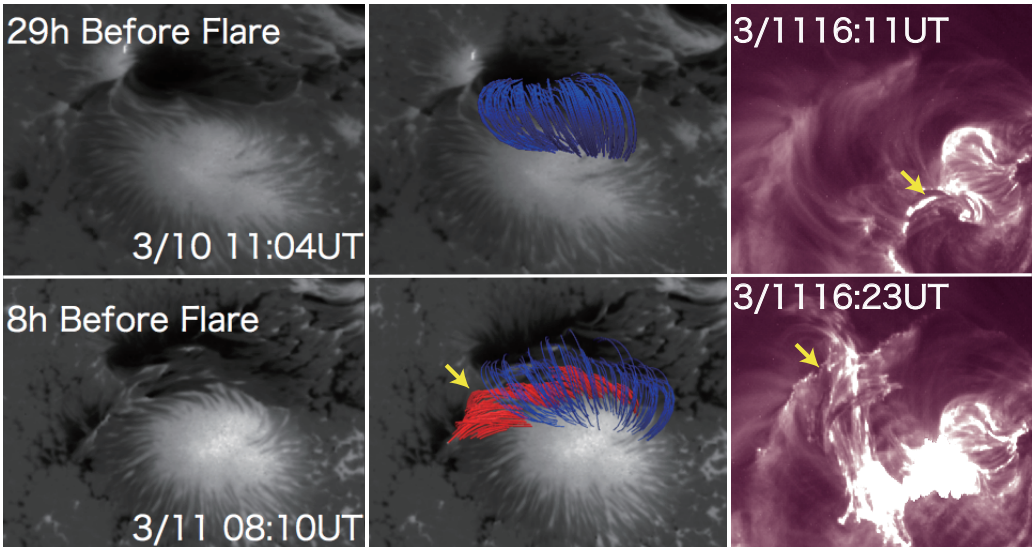

Figure 4.13: (Left column) Vertical magnetic field obtained by the *Hinode* SOT/SP at 11:04UT on 10th and at 08:10UT on 11th, respectively. White (black) color map in the background is positive (negative) vertical magnetic field. (Middle column) Corresponding 3-dimensional magnetic field extrapolated with the NLFFF method. Red lines are highly sheared magnetic field connecting P1 and N2b. Blue lines are potential like magnetic field connecting P1 and N2a. (Right column) AIA 211Å images before and after the CME onset.

4.4 Region 2 — 7 M-class Flares

4.4.1 Evolution of Magnetic Field, Magnetic Helicity and Associated Parameters

Now we focus on the evolution and flare occurrences in Region 2, that recurrently produced 7 M-class flares and no X-class flares. SDO/AIA EUV intensity images and HMI LOS magnetogram maps of these flares are shown in fig 4.14∼4.20.

Interestingly, the magnetic evolution in Region 2 is similar to that of Region 1. Fig. 4.21 shows 8 time slices of enlarged view of magnetic field evolution in Region 2. This region was mainly composed of 2 magnetic patches, one was the small negative sunspot N3 and the other was P2 which is the positive footpoint of the emerging flux P2-N2. Since P2 moved westward in the south of N3, this motion corresponds to the counter-clockwise mutual rotation between P2 and N3. Note that this region also contains P3 which is asso-

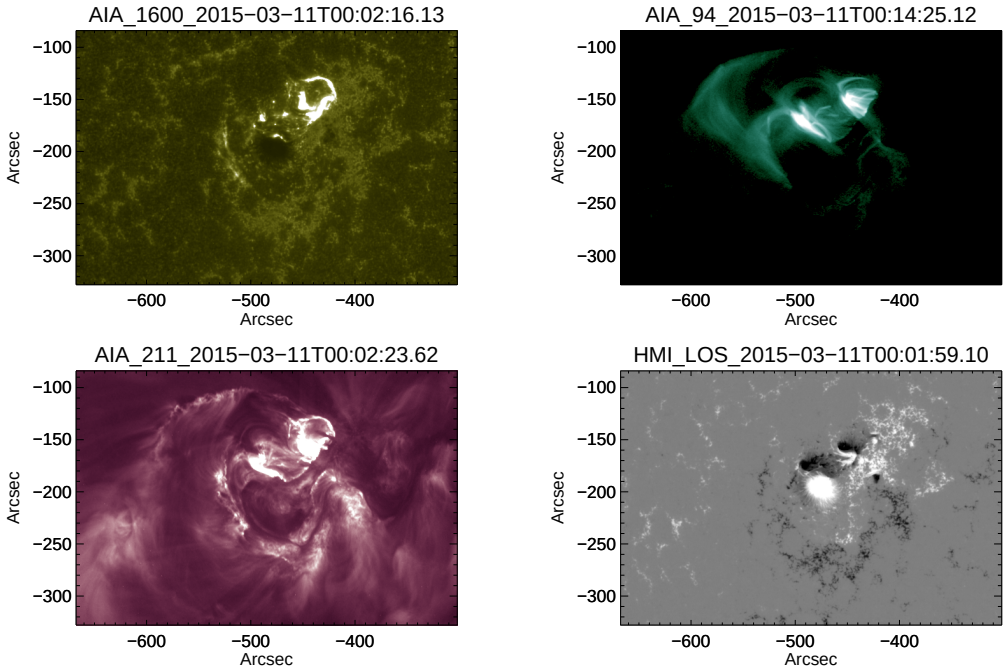

Figure 4.14: EUV images at the time of M2.9 flare taken by the AIA in the wavelength of (Top left) 1600Å, (Top right) 94Å and (Bottom left) 211Å. (Bottom right) The image of LOS magnetic field at the corresponding time.

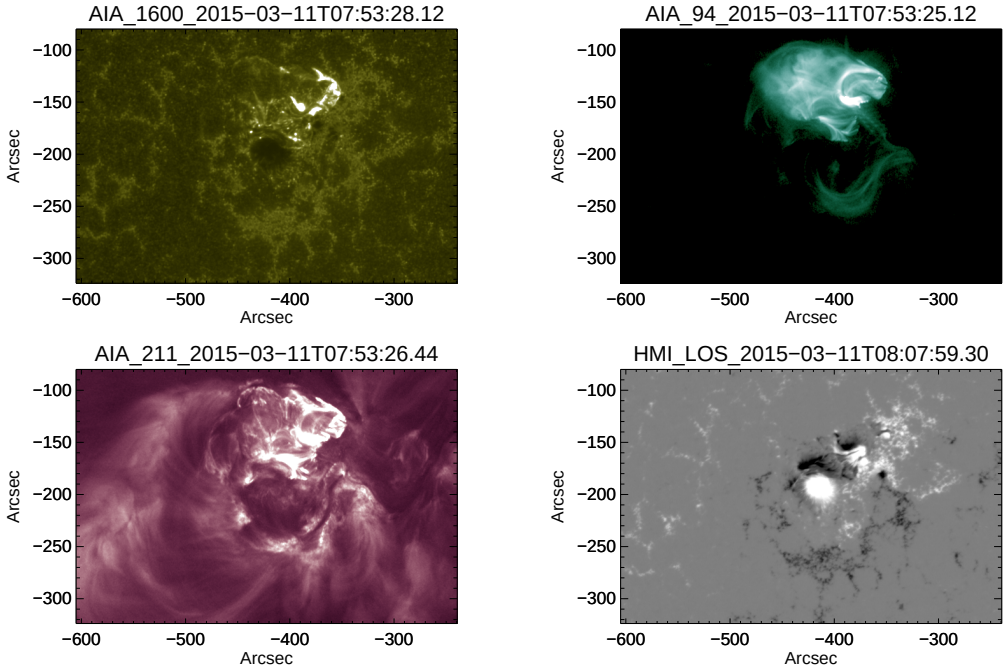

Figure 4.15: EUV images at the time of M2.6 flare taken by the AIA in the wavelength of (Top left) 1600Å, (Top right) 94Å and (Bottom left) 211Å. (Bottom right) The image of LOS magnetic field at the corresponding time.

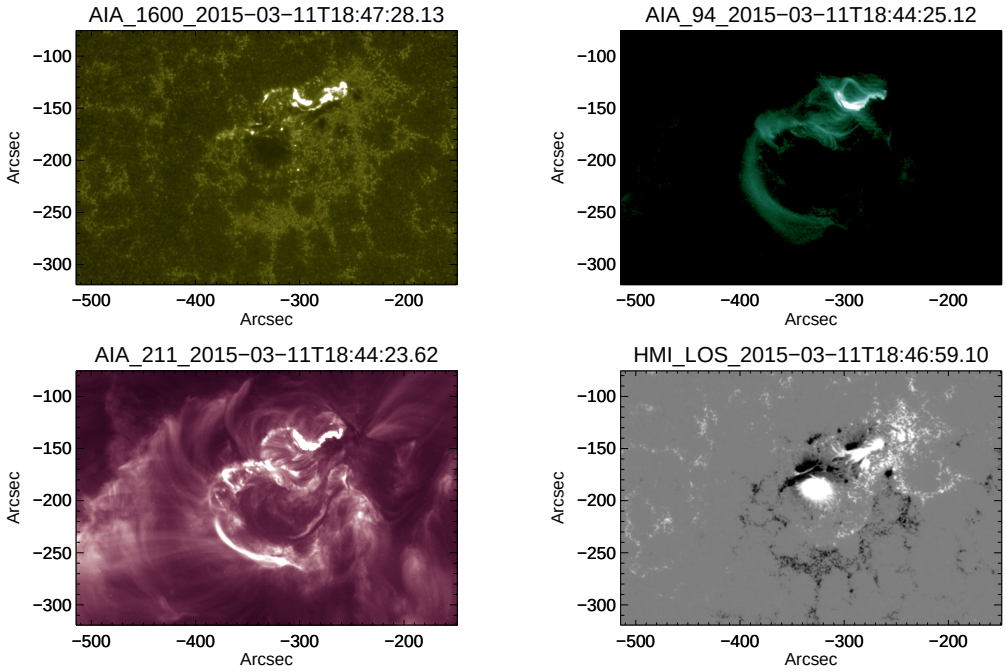

Figure 4.16: EUV images at the time of M1.0 flare taken by the AIA in the wavelength of (Top left) 1600Å, (Top right) 94Å and (Bottom left) 211Å. (Bottom right) The image of LOS magnetic field at the corresponding time.

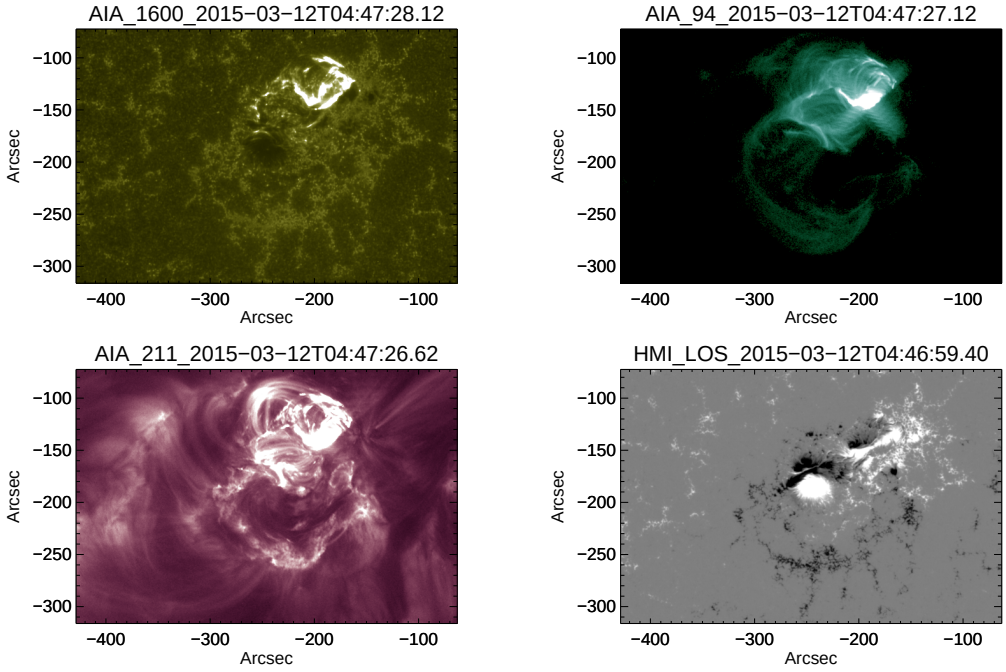

Figure 4.17: EUV images at the time of M3.2 flare taken by the AIA in the wavelength of (Top left) 1600Å, (Top right) 94Å and (Bottom left) 211Å. (Bottom right) The image of LOS magnetic field at the corresponding time.

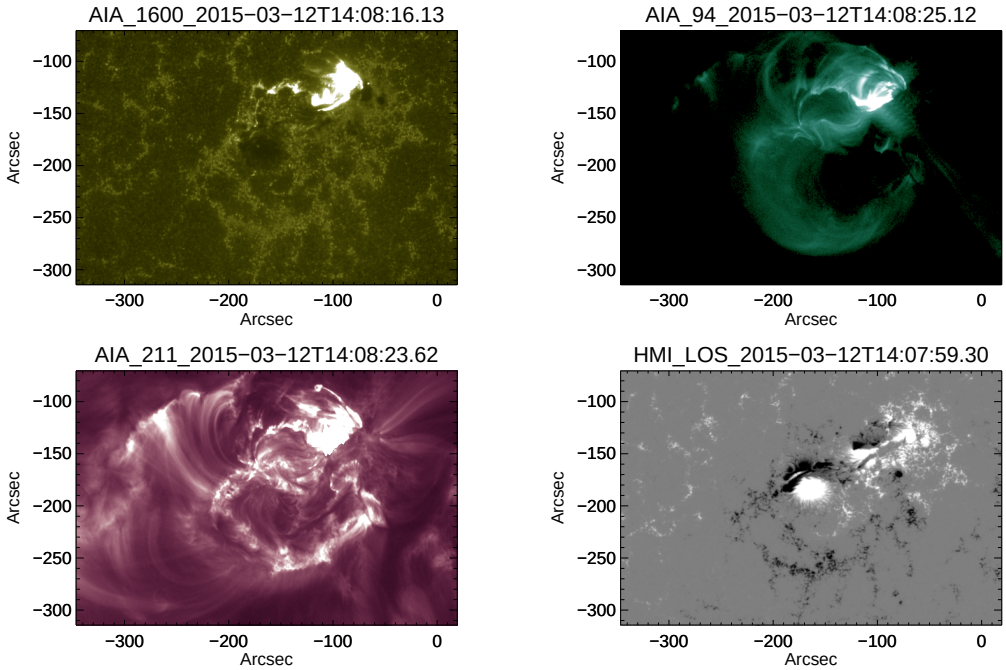

Figure 4.18: EUV images at the time of M4.2 flare taken by the AIA in the wavelength of (Top left) 1600Å, (Top right) 94Å and (Bottom left) 211Å. (Bottom right) The image of LOS magnetic field at the corresponding time.

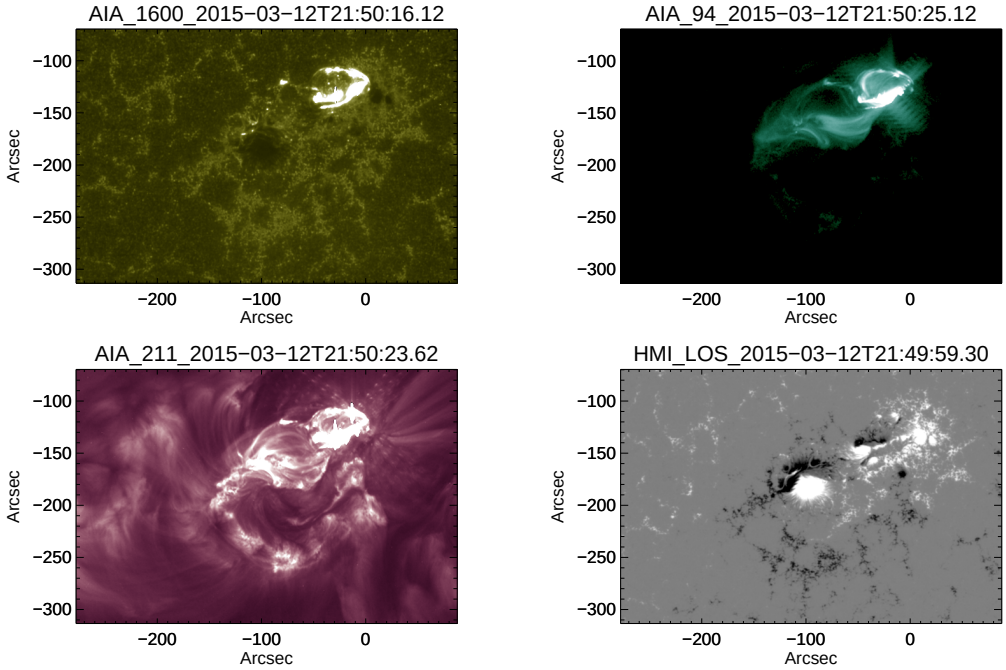

Figure 4.19: EUV images at the time of M2.7 flare taken by the AIA in the wavelength of (Top left) 1600Å, (Top right) 94Å and (Bottom left) 211Å. (Bottom right) The image of LOS magnetic field at the corresponding time.

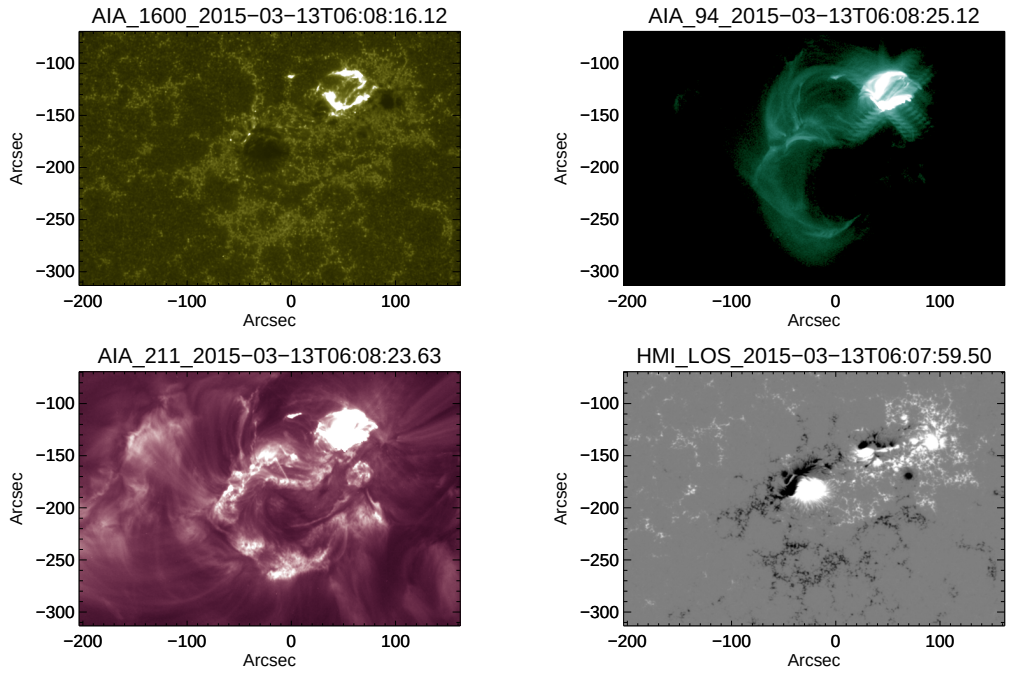

Figure 4.20: EUV images at the time of M1.8 flare taken by the AIA in the wavelength of (Top left) 1600Å, (Top right) 94Å and (Bottom left) 211Å. (Bottom right) The image of LOS magnetic field at the corresponding time.

ciated with N3.

Fig. 4.22 represents G_θ maps at corresponding time of fig. 4.21. Although the emerging flux sometimes injected negative magnetic helicity in the south of the spot, mainly the spot N3 and an emerging flux P2 injected positive magnetic helicity. In the case of Region 2, the small spot N3 did not show strong opposite helicity injection accompanied by emergence.

Fig. 4.23 shows the evolution of the same parameters as fig. 4.10. Practically, N3 is defined with the B_z threshold of -1000[G] and P2 is defined as the set of pixels having magnitude of B_z more than 1000[G] in the arbitrary box-shaped region. Parameters except for absolute magnetic fluxes (in panels (a) and (b)) are averaged over 1.5 hours.

The magnetic flux of the sunspot N3 was much smaller than the emerging flux P2 in Region 2. This is opposite to the case of Region 1 where the magnetic flux in the sunspot P1 was larger than emerging flux N2. In the studied period, the maximum absolute magnetic flux in N3 was $\sim 0.5 \times 10^{21} Mx$ and in P2 was $\sim 4 \times 10^{21} Mx$. Before the first

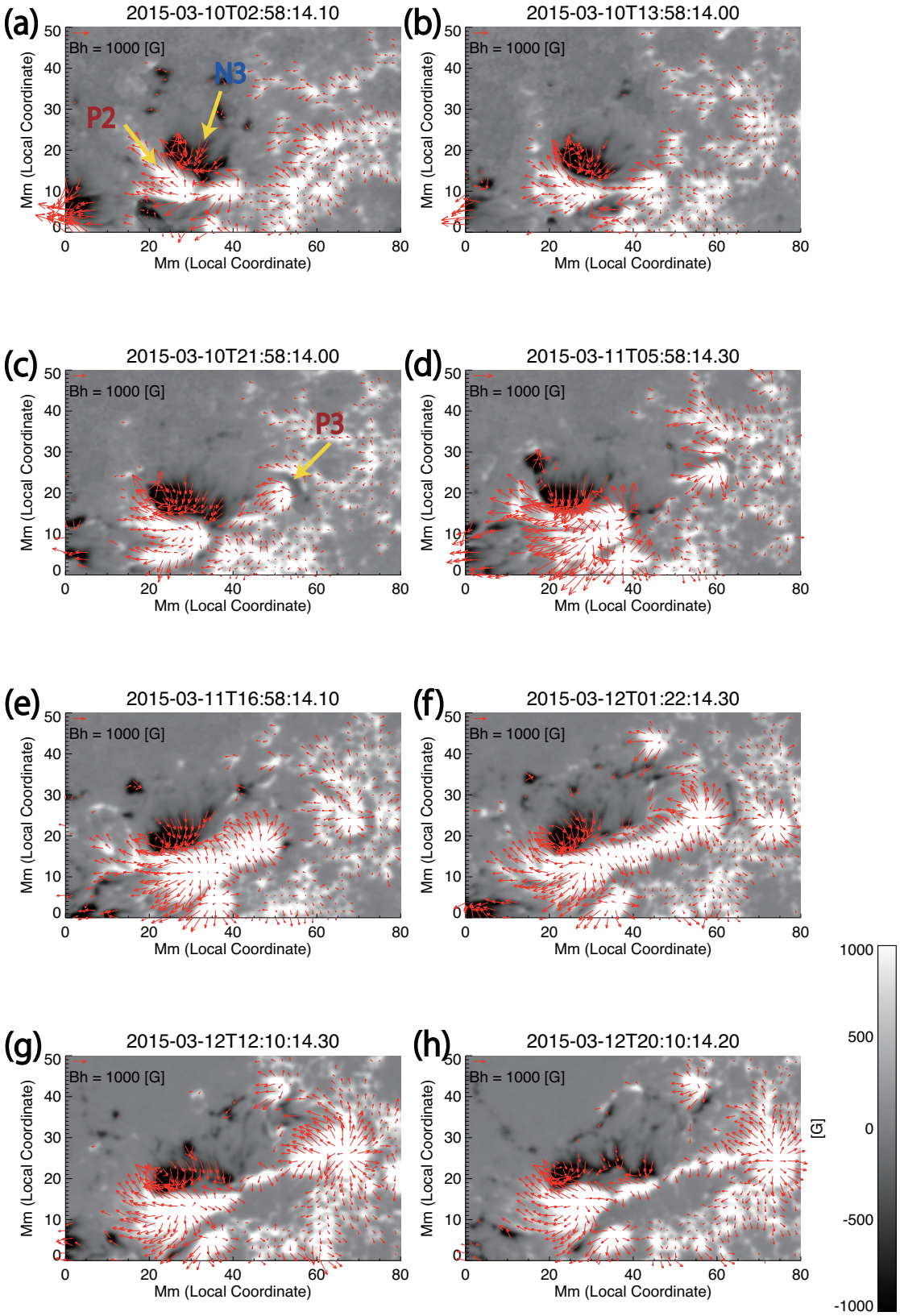

Figure 4.21: B_z maps enlarged in Region 2. The background color maps show the magnitude of vertical magnetic field obtained by HMI. Red arrows represent the horizontal magnetic field.

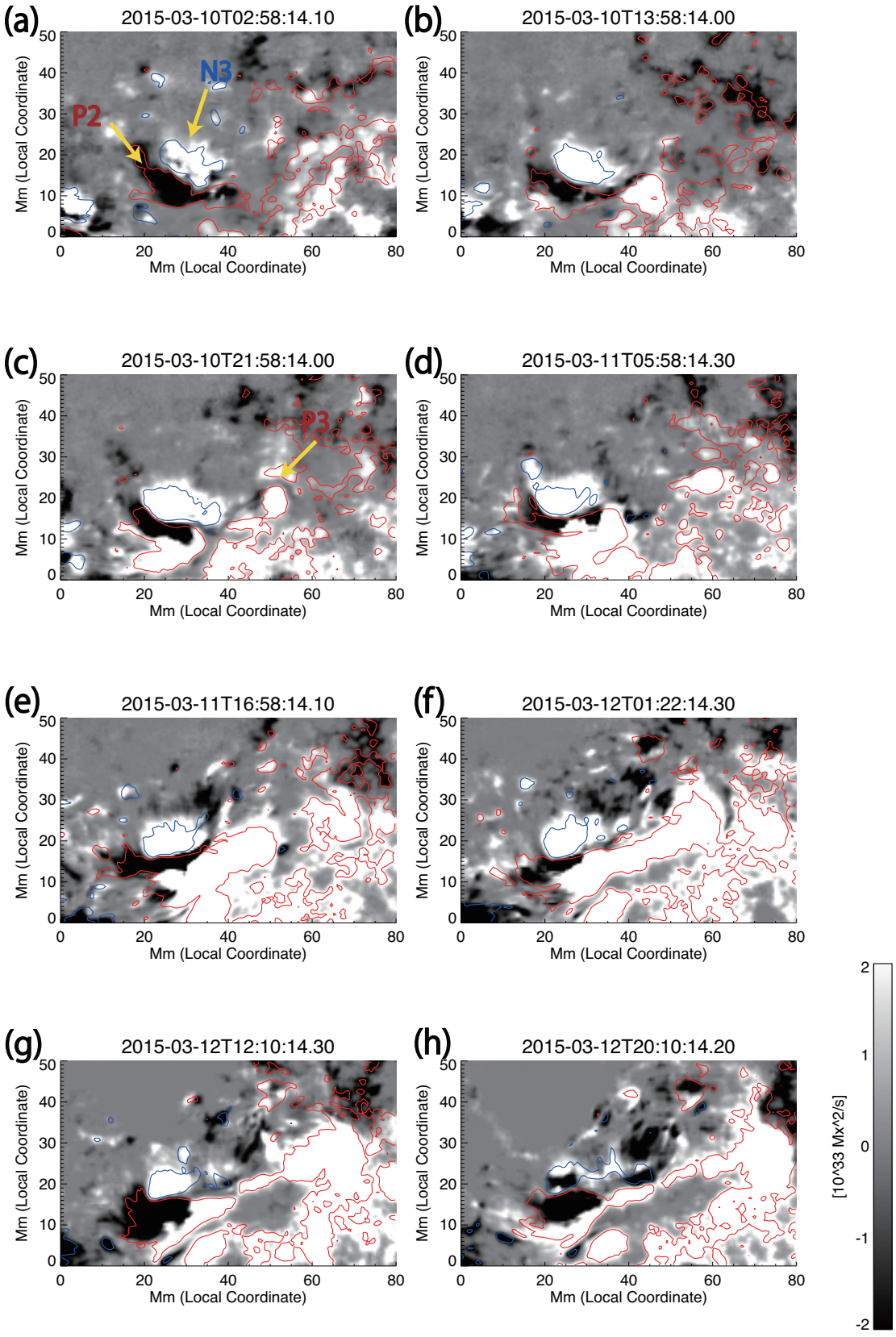

Figure 4.22: G_θ maps enlarged in Region 2. Red and blue contours represent $B_z = \pm 500[G]$.

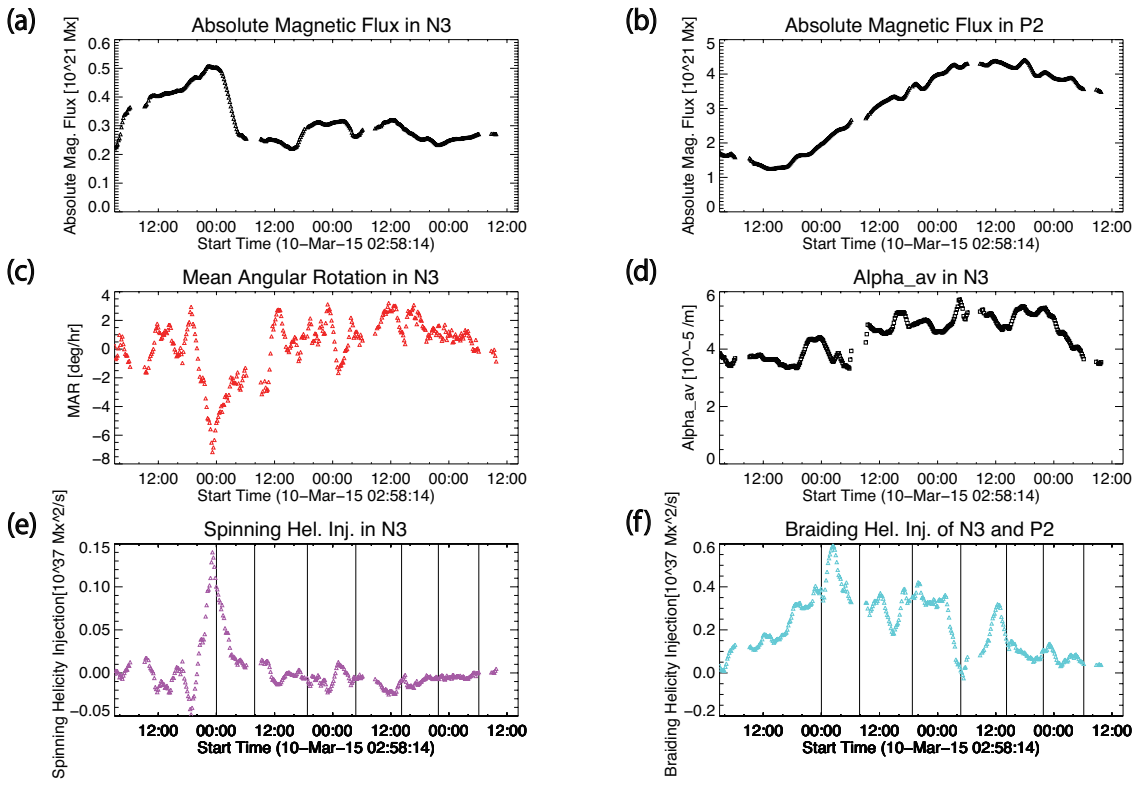

Figure 4.23: Temporal evolution of associated parameters in Region 2. (a) Absolute magnetic flux of a spot (N3), (b) absolute magnetic flux of an emerging flux (P2), (c) mean angular rotation of a spot (N3), (d) α_{av} in a spot (N3), (e) spinning helicity injection in a spot (N3), (f)braiding helicity injection between a spot (N3) and an emerging flux (P2). The vertical solid lines represent start time of M-class flares.

flare which occurred at 0UT on 11th, the absolute magnetic flux in N3 increased, thus N3 was in the emerging phase. A little later, positive spinning helicity was injected in N3. Magnetic flux in the sunspot N3 decreased sharply from 22UT on 10th, accompanied by the emergence of P2. This time profile implies that much magnetic flux in N3 and P2 was cancelled and newly connected flux between N3 and P2 submerged. Braiding helicity injection between P2 and N3 was much larger than spinning helicity injection in N3, a factor of ~ 20. Moreover, panels (d) and (f) of fig 4.23 show that α_{av} and braiding helicity injection display large fluctuation with time. This recursion is similar to that of M-class flare occurrences.

Regarding the rotation of the sunspot, fig. 4.23(c) shows that the small sunspot N3 started a rapid clockwise rotation from 19UT on 10th. This was delayed a bit from the time when the absolute magnetic flux started to increase in fig. 4.23(a) according to the emergence of N3. After a while, the flux cancellation mentioned above occurred. The fast clockwise of sunspot rotation did not continue so long and ended at 11UT on 11th. In the late phase, N3 had small but positive rotational rate, i.e. N3 rotated counter-clockwise.

4.4.2 Magnetic Connectivity in the Corona

Left column in fig. 4.24 corresponds to the vertical magnetic field obtained by the SOT/SP at 11:04UT on 10th, at 08:10UT on 11th, and at 10:37UT on 12th, respectively. Middle column in fig. 4.24 displays the corresponding 3-dimensional magnetic field reproduced by the NLFFF extrapolation. Blue lines represent arcade-like magnetic field between P3 and N3, and green field lines stand for coronal structure of the emerging flux whose footpoints in the photosphere are P2 and N2. At 11:04UT on 10th, between P2 and N3, highly sheared field was already formed (red). As P2 moved westward, red field lines were more sheared. However, at 10:37UT on 12th, N3 became elongated and red lines transformed into a low-energy arcade-like structure. Instead, relatively sheared structure was formed (yellow) in the north-west region.

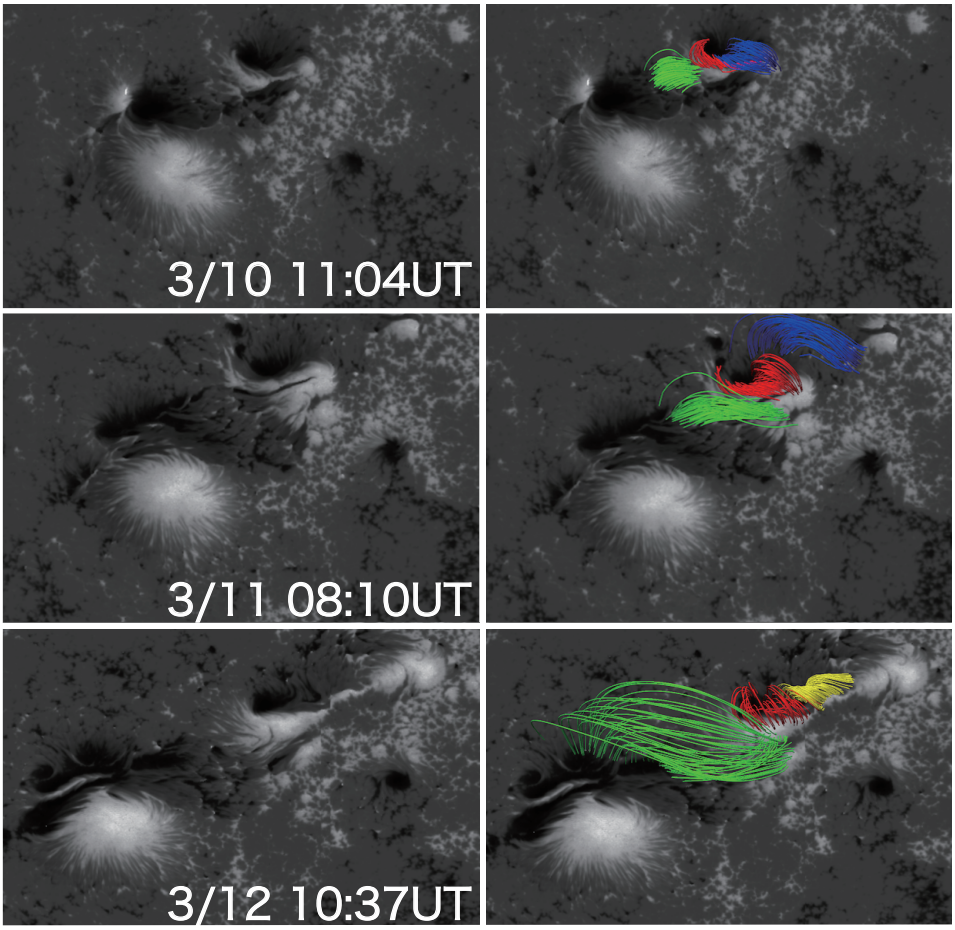

Figure 4.24: (Left column) Vertical magnetic field obtained by the *Hinode* SOT/SP at 11:04UT on 10th, at 08:10UT on 11th, and at 10:37UT on 12th, respectively. White (black) color map in the background is positive (negative) vertical magnetic field. (Right column) Corresponding 3-dimensional magnetic field extrapolated with NLFFF method. Field lines around the Region 2 are chosen. Blue lines represents arcade-like magnetic field between P3 and N3. Green field lines stand for the emerging flux and connects P2 and N2. Red and yellow lines are magnetic field connecting N3 and P2.

Chapter 5

Discussions

In this chapter, we discuss the results obtained by our analysis. First, we discuss the sunspot rotation and flaring patterns of Region 1 and 2 in Section 5.1. Second, we compare the results of our analysis on NOAA 12297 with previous studies on NOAA 10930 in Section 5.2. This active region produced an X3.4 flare in 2006 December and was studied in detail in different works. Finally, we present our future research plans in Section 5.3.

5.1 Comparison of Region 1 and Region 2

5.1.1 Sunspot Rotation

As shown in Chapter 4, Region 1 and 2 displayed different flaring activities. In Region 1, the largest flare of this active region (i.e. an X2.1 flare) occurred. On the other hand, in Region 2, M-class flares frequently took place.

In the analysis of Region 1, we identified the rotational reversal of the largest sunspot P1 as a precursor of the X2.1 flare. Though P1 rotated clockwise before 22UT on 10th, P1 showed counter-clockwise rotation accompanied by the fast flux emergence of N2b. Due to the rotation, P1 injected opposite (negative) magnetic helicity to the global (positive) one. However, α_{av} was still positive and increased after the rotational reversal. Therefore, magnetic and current helicity showed different sign evolution.

We consider the mechanism responsible for the reversed rotation as fig. 5.1. In this schematics, the rotation of P1 was associated with fast development of N2b due to the flux emergence. When a sunspot in the southern hemisphere rotates following the hemispheric rule in terms of magnetic helicity as shown in fig.1.9, this sunspot with clockwise spiral (positive current helicity) rotates clockwise and injects positive magnetic helicity as explained in fig.5.1(a). In this case, the rotation is apparent motion due to the vertical motion of twisted flux tube, or is driven by the internal magnetic force due to an imbalance of Lorentz torque as described in Section 1.3. On the other hand, the reversed rotation of P1 was caused by rapid emergence of N2b externally. As shown in fig. 5.1(b), when a sunspot with positive current helicity is forced to rotate by an external force, the rotational direction is counter-clockwise and the dextral spiral is enhanced, then current helicity increases. This picture is consistent with our analysis of P1.

There are 2 candidates of external force which rotated the sunspot P1 reversely. One is that the emergence of N2b caused a strong eastward plasma flow that pushed the north part of P1. In other words, the sunspot was forced to rotate by the kinetic force. Another option is that during emergence of N2b, reconnection gradually occurred and connected P1 and N2b, subsequent eastward motion of N2b dragged P1's penumbral magnetic field, and forced P1 to rotate counter-clockwise. In the latter case, the magnetic tension force rotated the sunspot, and this picture is consistent with the result that the connectivity between P1 and N2b was newly formed as fig. 4.13 shows. As future works, it must be identified which mechanism, namely, magnetic tension force or kinetic energy of plasma flow can explain the behavior of the sunspot rotation quantitatively. It should be noted that the subsurface dynamo effect is not considered in this picture.

Concerning Region 2, the pre-existing small sunspot N3 had clockwise spiral structure, as shown in Figure 5.2. The emergence of P2 did not cause a counter-clockwise rotation of N3 in the early phase. We believe that it is because N3 was in the emerging phase and the internal force overcame the external force by P2's emergence as shown in fig. 5.2. Fig. 4.23(a) displays that magnetic flux in N3 increased till 0UT on 11th. During

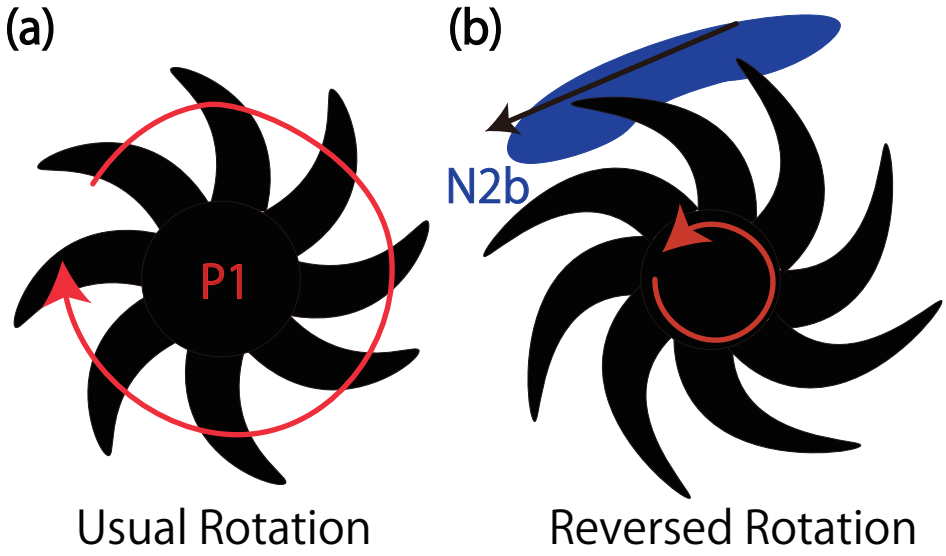

Figure 5.1: Schematic picture of sunspot rotation in Region 1. (left) Schematics of sunspot rotation in the southern hemisphere injecting positive magnetic helicity following the hemispheric rule. (right) Sunspot rotating counter-clockwise in our case. The rotation is forced by the external factors.

that period the spinning helicity injection in N3 tended to be positive although it fluctuated. Moreover, soon after the emergence of P2, the magnetic flux in N3 experienced strong magnetic cancellation with a part of positive polarity flux in P2. Hence, if a new connection between N3 and P2 was formed, it might submerge and be cancelled. Note that, after 12UT on 11th, N3 tended to rotate counter-clockwise weakly. This is a similar behavior to the case of reversed rotation as fig 5.1(b).

5.1.2 Difference in Helicity Injection and Flare Occurrences

Region 1 and 2 showed different behavior regarding the evolution of the helicity injection. In Region 1, the negative spinning helicity was injected before the X2.1 flare occurred. In Region 2, the positive braiding helicity was injected recurrently while M-class flares successively occurred. These behaviors of helicity injection in Region 1 and 2 are consistent with flaring activities in each region.

The most significant feature of the helicity evolution in Region 1 was the large amount of negative spinning helicity injection in P1. This is consistent with the model where the

Figure 5.2: Schematic picture of sunspot rotation in the early phase in Region2.

annihilation of positive and negative helicity triggers a large flare (Kusano et al., 2003). From the point of view of free energy build-up, this opposite helicity injection means that the amount of free energy decreases. We consider that the decrease of free energy is the reason why the number of flares larger than M-class was small in spite of strong magnetic field in Region 1. However, it should be noted that, generally, the relation between the amount of free energy and that of magnetic helicity is not straightforward as Eq. (1.17), especially when magnetic field structure has positive and negative magnetic helicity at the same time. Before the X2.1 flare, α_{av} in Region 1 drastically increased owing to the reversed rotation by the external force. This means that the local twist was enhanced when the X-class flare occurred. The increase of local twist might affect on the CME ejection producing a helical motion accompanied by the X2.1 flare. This CME onset meets the result by Park et al. (2012) that non-monotonic helicity accumulation tends to produce large and fast CMEs.

On the other hand, the helicity evolution in Region 2 was characterized by fluctuating braiding helicity injection by emergence of P2. This oscillating time profile implies recurrent energy input into Region 2 and it is consistent with recurrent occurrences of flares. Moreover, the combination of clockwise self-rotation and counter-clockwise mu-

tual rotation, which was seen in the early phase of the evolution in Region 2, is the best scenario to inject positive magnetic helicity and to make sheared structure. Since positive magnetic helicity was successively injected into Region 2, large flares also successively occurred. However, since the volume of the region and associated magnetic flux were small in Region 2, the magnitude of these flares might be lower than X-class.

5.2 Comparison with Previous Observations: NOAA 10930

The results of this thesis can be compared with previous studies on NOAA 10930. This active region produced an X3.4 flare and is one of the most studied active region from various points of view. In this regard, although there is a difference that NOAA 10930 was a negative helicity active region (Su et al., 2009) despite of its location in the southern hemisphere (then this active region violated the hemispheric rule), these regions have many features of their evolution in common, as shown in fig 5.3. NOAA 10930 had a similar configuration to that of Region 1 of NOAA 12297 we studied. This active region was constituted of a large negative sunspot and a small positive sunspot (Kubo et al., 2007). In the middle of its evolution, the size and magnetic flux increased in the small sunspot and it moved clockwise to the large sunspot. Accompanied by this motion, the large sunspot changed the sign of magnetic helicity injection from negative to positive (Park et al., 2010). Self-rotational direction of the big sunspot also changed from counter-clockwise to clockwise two times (Ravindra et al., 2011). The clockwise direction is the same as the direction of mutual rotation between a big spot and a small spot. Speed of the reversed rotation reached 1 $[deg/hr]$. The rotational rate is about a half of that of reversed rotation we analyzed. Magara & Tsuneta (2008) pointed out that NOAA 10930 showed the saturation in the time profile of magnetic helicity accumulation. This time profile is similar to that shown in fig. 4.11. The X3.4 flare occurred after these features were detected. This

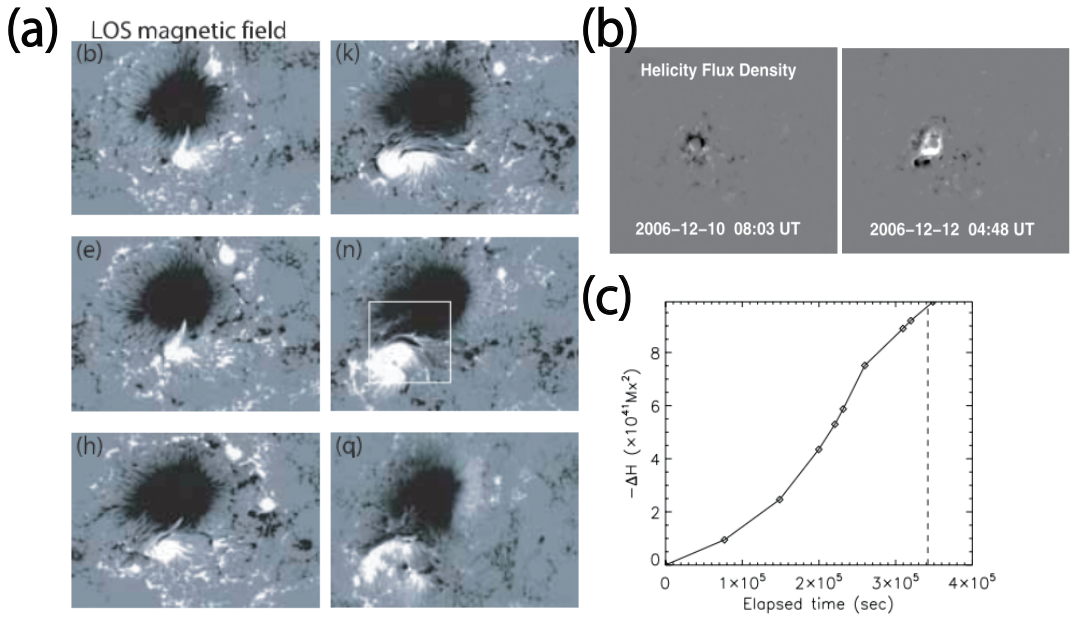

Figure 5.3: (a) Evolution of LOS magnetic field in NOAA 10930. Images are from Kubo et al. (2007). (b) Opposite magnetic helicity injection in a big spot from (left) negative to (right) positive. Images are from Park et al. (2010). (c) Magnetic helicity accumulation shows relatively flat time profile before the X3.4 flare, as obtained in the analysis of NOAA 12297. Image is from Magara & Tsuneta (2008).

comparison implies that the properties of magnetic field evolution seen in NOAA 10930 and 12297 have important roles on the trigger of large solar flares.

5.3 Future Research

In this discussion, we propose the picture of reversed sunspot rotation by external forces. The picture lacks the quantitative evaluation of how much the kinetic energy or magnetic tension force can rotate a sunspot reversely. Subsurface response to rotational reversal is also not considered. These problems should be studied in future works.

The effect on the corona of reversed sunspot rotation cannot be fully understood only by our observations. For further understanding of the process we think it is insightful to perform numerical simulation of opposite helicity injection into an bipolar magnetic field by forcing its footpoints to rotate reversely and to investigate the coronal response.

It is pointed out that deduction of flow velocity field in the strong magnetic field region

(e.g. the center of sunspot) with an optical flow method is relatively inaccurate. We need to develop more accurate methods to remove spurious signals.

Another work we should do is an active region survey about spinning, braiding helicity injection, and sunspot rotation, and check the correspondence to the hemispheric rule. Also, we have to compare the survey with magnitude and frequency of flares and to verify our results for NOAA 12297.

Chapter 6

Summary

To reveal the relationship between flares and magnetic field evolution, we study the magnetic helicity injection, and self and mutual sunspot rotations. We focus on NOAA 12297 which is suitable for our flare study because this active region was flare-productive and close to solar disc center.

We analyze this active region with the optical flow method 'DAVE', survey of parameters associated with complexity of magnetic field, and the NLFFF extrapolation. As associated parameters, we estimate magnetic flux of sunspots and emerging fluxes, magnetic helicity accumulation, magnetic helicity flux density G_θ, average force-free alpha α_{av}, spinning and braiding helicity injection, and rotational rate of sunspots.

We identify 2 flare-productive regions labelled as Region 1 and 2 which showed different flaring patterns. Region 1 produced an X2.1 flare and Region 2 generated 7 M-class flares. We focus on the similar configuration of their magnetic field evolution. Both regions contained a footpoint of an emerging flux rotating counter-clockwise to a spot.

In Region 1, we identify the change of the sign of helicity injection from positive to negative in a large sunspot (P1) before the X-class flare occurred. This opposite helicity injection started accompanied by fast emergence of a part of emerging fluxes (N2b). The absolute value of negative spinning helicity injection in P1 was larger than that of positive braiding helicity injection between P1 and emerging fluxes (N2). In spite of this opposite

helicity injection, current helicity (α_{av}) in P1 was still positive and increased with time. On the other hand, oscillating braiding helicity injection between a small sunspot (N3) and emerging fluxes (P2) was a significant feature in Region 2. The absolute value of braiding helicity injection between N3 and P2 was much larger than spinning helicity injection in N3. N3 did not show negative spinning when P2 started to emerge. However, in the late phase of the emergence, spinning helicity injection was small and negative.

The strong opposite helicity injection as a precursor of a large flare in Region 1 is consistent with the flare model of helicity annihilation. The sign reversal of spinning helicity injection from positive to negative corresponds to the rotational reversal from clockwise to counter-clockwise. We interpret the sign reversal in P1 as following; P1 was forced to rotate reversely by an external force due to the N2b's emergence. This picture explains why the evolution of α_{av} was different from that of magnetic helicity injection. Furthermore, the fluctuating braiding helicity injection in Region 2 implies the recurrent energy input. This is consistent with successive occurrences of M-class flares. The spot N3 did not show rotational reversal when emerging fluxes appeared. We consider the reason is that N3 was in the emerging phase and the internal force overcame the external force by the emergence of P2. Our results show that a manner of helicity injection has an important role on determining frequency and magnitude of flares.

Based on the results, we will investigate roles of magnetic helicity more profoundly in the future. We will survey spinning and braiding helicity injection in flare-productive active regions to verify our results. Moreover, we will carry out numerical MHD simulation and investigate the coronal response of reversed rotation at footpoints of a bipole.

Acknowledgments

I would like to express a great deal of appreciation to my supervisor Prof. Toshifumi Shimizu for his kind supports and insightful discussions. I deeply appreciate supports and fruitful suggestions from members of my group, T. Sakao, K. Matsuzaki, K. Daiguji, I. Yamagishi, C. Q. Noda, S. Ishikawa, Y. Bamba, T. Kawate, D. H. Brooks, T. Oba, Y. Kawabata, T. Doi and M. Abe. My colleagues, C. Q. Noda and T. Oba kindly revised the draft of this thesis. I'm profoundly grateful to Dr. Satoshi Inoue, who developed the NLFFF code, that he accepted me to use his code in our study. Finally, I want to show my sincere gratitude to my family for their encouragements and cordial supports.

The HMI and AIA data used in this thesis are courtesy of NASA/SDO and the AIA and HMI science team. $Hinode$ is a Japanese mission developed and launched by ISAS/JAXA, with NAOJ as a domestic partner and NASA and STFC (UK) as international partners. It is operated by these agencies in co-operation with ESA and NSC (Norway). I'm grateful to people involved in these missions.

This work uses the DAVE codes written and developed by the Naval Research Laboratory. Numerical computations were performed on Supercomputer for earth Observation, Rockets and Aeronautics (SORA) of JAXA. Visualization of 3-dimensional magnetic field is done with UCAR's VAPOR visualization package (www.vapor.ucar.edu).

References

Amari, T., Luciani, J. F., Aly, J. J., & Tagger, M. 1996, The Astrophysical Journal, 466, L39

Archontis, V., Hood, A. W., Savcheva, A., Golub, L., & Deluca, E. 2009, Astrophysical Journal, 691, 1276

Barnes, C., & Sturrock, P. 1972, The Astrophysical Journal, 174, 659

Berger, M. A., & Field, G. B. 1984, J. Fluid. Mech., 147, 133

Borrero, J. M., Tomczyk, S., Kubo, M., Socas-Navarro, H., Schou, J., Couvidat, S., & Bogart, R. 2011, Solar Physics, 273, 267

Brown, D. S., Nightingale, R. W., Alexander, D., Schrijver, C. J., Metcalf, T. R., Shine, R. A., Title, A. M., & Wolfson, C. J. 2003, Solar Physics, 216, 79

Calabretta, M. R., & Greisen, E. W. 2002, Astronomy & Astrophysics, 395, 1077

Carmichael, H. 1964, The Physics of Solar Flares, 50, 451

Chae, J., Moon, Y. J., Rust, D. M., Wang, H., & Goode, P. R. 2003, Journal of The Korean Astronomical Society, 36, 33

Chae, J., Wang, H., Qiu, J., Goode, P. R., Strous, L., & Yun, H. S. 2001, The Astrophysical Journal, 560, 476

Dedner, A., Kemm, F., Kröner, D., Munz, C. D., Schnitzer, T., & Wesenberg, M. 2002, Journal of Computational Physics, 175, 645

Démoulin, P., & Berger, M. A. 2003, Solar Physics, 215, 203

Démoulin, P., Mandrini, C. H., Van Driel-Gesztelyi, L., Lopez Fuentes, M. C., & Aulanier, G. 2002, Solar Physics, 207, 87

Evershed, J. 1909, Monthly Notices of the Royal Astronomical Society, 69, 454

—. 1910, Monthly Notices of the Royal Astronomical Society, 70, 217

Fan, Y. 2009, The Astrophysical Journal, 697, 1529

Finn, J., & Antonsen Jr., T. 1985, Comments Plasma Phys. Control. Fusion, 9, 111

Frisch, U., Pouquet, A., Léorat, J., & Mazure, A. 1975, Journal of Fluid Mechanics, 68, 769

Gary, G. A. 2001, Solar Physics, 203, 71

Gibson, S. E., Fan, Y., Mandrini, C., Fisher, G., & Demoulin, P. 2004, The Astrophysical Journal, 617, 600

Hagino, M., & Sakurai, T. 2004, Publications of the Astronomical Society of Japan, 56, 831

Hirayama, T. 1974, Solar Physics, 34, 323

Holder, Z. A., Canfield, R. C., Mcmullen, R. A., Nandy, D., Howard, R. F., & Pevtsov, A. A. 2004, The Astrophysical Journal, 611, 1149

Ichimoto, K., et al. 2008, Solar Physics, 249, 233

Inoue, S., Magara, T., Pandey, V. S., Shiota, D., Kusano, K., Choe, G. S., & Kim, K. S. 2014, The Astrophysical Journal, 780, 101

Kazachenko, M. D., Canfield, R. C., Longcope, D. W., & Qiu, J. 2010, Astrophysical Journal, 722, 1539

Knoska, S. 1975, Astronomical Institutes of Czechoslovakia, 26, 151

Kopp, R., & Pneuman, G. 1976, Solar Physics, 50, 85

Kosugi, T., et al. 2007, Solar Physics, 243, 3

Kubo, M., et al. 2007, Publications of the Astronomical Society of Japan, 59, 779

Kusano, K., Bamba, Y., Yamamoto, T. T., Iida, Y., Toriumi, S., & Asai, A. 2012, The Astrophysical Journal, 760, 31

Kusano, K., Maeshiro, T., Yokoyama, T., & Sakurai, T. 2002, The Astrophysical Journal, 577, 501

Kusano, K., Suzuki, Y., & Nishikawa, K. 1995, The Astrophysical Journal, 441, 942

Kusano, K., Yokoyama, T., Maeshiro, T., & Sakurai, T. 2003, Advances in Space Research, 32, 1931

Leka, K. D., Barnes, G., & Crouch, A. 2009, The Second HINODE Science Meeting, 365

Lemen, J., et al. 2012, Solar Physics, 275, 17

Lites, B. W., & Ichimoto, K. 2013, Solar Physics, 283, 601

Lites, B. W., et al. 2013, Solar Physics, 283, 579

Longcope, D., Linton, M., Pevtsov, A., & Klapper, I. 1999, Geophysical Monograph, 2

Longcope, D. W., Ravindra, B., & Barnes, G. 2007, The Astrophysical Journal, 668, 571

Longcope, D. W., & Welsch, B. T. 2000, The Astrophysical Journal, 545, 1089

Magara, T. 2006, The Astrophysical Journal, 653, 1499

Magara, T., & Tsuneta, S. 2008, Publications of the Astronomical Society of Japan, 60, 1181

Matthaeus, W. H. 1982, Geophysical Research Letters, 9, 660

Metcalf, T. R. 1994, Solar Physics, 155, 235

Metcalf, T. R., Jiao, L., Alexander, N., Canfield, R., & Uitenbroek, H. 1995, The Astrophysical Journal, 439, 474

Min, S., & Chae, J. 2009, Solar Physics, 258, 203

November, L. J., & Simon, G. W. 1988, The Astrophysical Journal, 333, 427

Pariat, E., Démoulin, P., & Berger, M. A. 2005, Astronomy & Astrophysics, 439, 1191

Park, S.-H., Chae, J., Jing, J., Tan, C., & Wang, H. 2010, The Astrophysical Journal, 720, 1102

Park, S.-H., Cho, K.-S., Bong, S.-C., Kumar, P., Chae, J., Liu, R., & Wang, H. 2012, The Astrophysical Journal, 750, 48

Park, S.-H., et al. 2013, The Astrophysical Journal, 778, 13

Pesnell, W. D., Chamberlin, P., & Thompson, B. 2012, Solar Physics, 275, 3

Pevtsov, A. 1995, The Astrophysical Journal, 440, 109

Pevtsov, A. A. 2002, inCOSPARColloq. Ser. 13,Multi-Wavelength Observations of Coronal Structure and Dynamics, ed. P. C. H. Martens & D. P. Cauffman (Amsterdam: Pergamon), 125

Pouquet, A., Frisch, U., & Léorat, J. 1976, Journal of Fluid Mechanics, 77, 321

Ravindra, B., Yoshimura, K., & Dasso, S. 2011, The Astrophysical Journal, 743, 33

Régnier, S., & Canfield, R. C. 2006, Astronomy and Astrophysics, 451, 319

Richardson, R. S. 1941, The Astrophysical Journal, 93, 24

Schou, J., et al. 2012, Solar Physics, 275, 229

Schrijver, C. J., et al. 2008, The Astrophysical Journal, 675, 1637

Schuck, P. W. 2005, The Astrophysical Journal, 632, 53

—. 2006, The Astrophysical Journal, 30

Schumidt, H. 1964, Ness W.N. (ed.) ASS-NASA Symposium on the Physics of Solar Flares., NASA SP-50, 107

Shibata, K., Masuda, S., Shimojo, M., Hara, H., Yokoyama, T., Tsuneta, S., Kosugi, T., & Ogawara, Y. 1995, The Astrophysical Journal, 451, 83

Shimizu, T., et al. 2008, Solar Physics, 249, 221

Stenflo, J. 1969, Solar Physics, 8, 115

Sturrock, P. 1966, Nature, 211, 695

Sturrock, P., Weber, M., Wheatland, M., & Wolfson, R. 2001, The Astrophysical Journal, 548, 492

Sturrock, Z., & Hood, A. W. 2016, Astronomy & Astrophysics, 63, 1

Sturrock, Z., Hood, A. W., Archontis, V., & Mcneill, C. M. 2015, Astronomy & Astrophysics, 582

Su, Y., van Ballegooijen, A., Lites, B. W., Deluca, E. E., Golub, L., Grigis, P. C., Huang, G., & Ji, H. 2009, The Astrophysical Journal, 691, 105

Suematsu, Y., et al. 2008, Solar Physics, 249, 197

Sun, X. 2013, arXiv, 1309, 2392

Suryanarayana, G. S. 2010, New Astronomy, 15, 313

Taylor, J. B. 1974, Physical Review Letters, 33, 1139

Tian, L., & Alexander, D. 2006, Solar Physics, 233, 29

—. 2008, The Astrophysical Journal, 673, 532

Tokman, M., & Bellan, P. M. 2002, The Astrophysical Journal, 567, 1202

Toriumi, S., & Takasao, S. 2017, The Astrophysical Journal, 850, 39

Torok, T., & Kliem, B. 2003, Astronomy and Astrophysics, 406, 1043

Török, T., & Kliem, B. 2005, The Astrophysical Journal, 630, L97

Tsuneta, S., et al. 2008, Solar Physics, 249, 167

Vemareddy, P., Ambastha, A., & Maurya, R. A. 2012, The Astrophysical Journal, 761, 60

Yan, X. L., Qu, Z. Q., & Xu, C. L. 2008, The Astrophysical Journal, 682, L65

Zhang, J., Li, L., & Song, Q. 2007, The Astrophysical Journal, 662, 35

Zhang, Y., Tan, B., & Yan, Y. 2008, The Astrophysical Journal, 682, L133

Zheng, J., Yang, Z., Guo, K., Wang, H., & Wang, S. 2016, The Astrophysical Journal, 826, 1